



HAL
open science

Films in narrow tubes

Georg F. Dietze, Christian Ruyer-Quil

► **To cite this version:**

Georg F. Dietze, Christian Ruyer-Quil. Films in narrow tubes. *Journal of Fluid Mechanics*, 2014, 762, pp.68-109. <10.1017/jfm.2014.648>. <hal-04437853>

HAL Id: hal-04437853

<https://hal.science/hal-04437853v1>

Submitted on 5 Feb 2024

HAL is a multi-disciplinary open access archive for the deposit and dissemination of scientific research documents, whether they are published or not. The documents may come from teaching and research institutions in France or abroad, or from public or private research centers.

L'archive ouverte pluridisciplinaire **HAL**, est destinée au dépôt et à la diffusion de documents scientifiques de niveau recherche, publiés ou non, émanant des établissements d'enseignement et de recherche français ou étrangers, des laboratoires publics ou privés.



HAL Authorization

Films in narrow tubes

GEORG F. DIETZE^{1,†} AND C. RUYER-QUIL^{2,3}

¹Univ. Paris-Sud, CNRS, Lab. FAST, Bât. 502, Campus Univ., Orsay, F-91405, France

²Universite de Savoie, CNRS - Lab. LOCIE, F-73376 Le Bourget du Lac, France

³Institut Universitaire de France

(Received 3 November 2014)

We consider the axisymmetric arrangement of an annular liquid film, coating the inner surface of a narrow cylindrical tube, in interaction with an active core-fluid. We introduce a low-dimensional model based on the two-phase Weighted Residual Integral Boundary Layer formalism (*J. Fluid Mech.*, vol. 722, 2013, pp. 348-393) which is able to capture the long-wave instabilities characterizing such flows. Our model improves upon existing works by fully representing interfacial coupling and accounting for inertia as well as streamwise viscous diffusion in both phases. We apply this model to gravity-free liquid-film/core-fluid arrangements in narrow capillaries with specific attention to the dynamics leading to flooding, i.e. when the liquid film drains into large-amplitude collars that occlude the tube cross-section. We do this against the background of linear stability calculations and non-linear two-phase direct numerical simulations. Thanks to the improvements of our model, we have found a number of novel/salient physical features of these flows. Firstly, we show that accounting for inertia and full inter-phase coupling is essential to capture the temporal evolution of flooding for fluid combinations that are not dominated by viscosity, e.g. water/air and water/silicone-oil. Secondly, we elucidate a viscous-blocking mechanism that drastically delays flooding in thin films which are too thick to form unduloids. This mechanism involves buckling of the residual film between two liquid collars, generating two very pronounced film troughs where viscous dissipation is drastically increased and growth effectively arrested. Only at very long times, breaking of symmetry in this region (due to small perturbations) initiates a sliding motion of the liquid film similar to observations by Lister et al. (*J. Fluid Mech.*, vol. 552, 2006, pp. 311-343) in thin non-flooding films. This kick-starts the growth of liquid collars anew and ultimately leads to flooding. We show that streamwise viscous diffusion is essential to this mechanism. Low-frequency core flow oscillations, such as occur in human pulmonary capillaries, are found to set off this sliding-induced flooding mechanism much earlier.

Key words: interfacial flows (free-surface), low-dimensional models, thin films

1. Introduction

The axisymmetric flow of an annular-liquid-film/fluid-core within a cylindrical tube, as shown in figure 1, can be viewed in different limits. In the simplest case, figure 1(a), the two-phase configuration is not subjected to gravity, which can be achieved either in a microgravity environment or in very narrow tubes. If, in addition, the core phase is quiescent, the film remains “static” in a noise-free environment, but is unstable to long-wave disturbances due to the Plateau-Rayleigh instability (Rayleigh 1892; Goren 1962),

† Email address for correspondence: dietze@fast.u-psud.fr

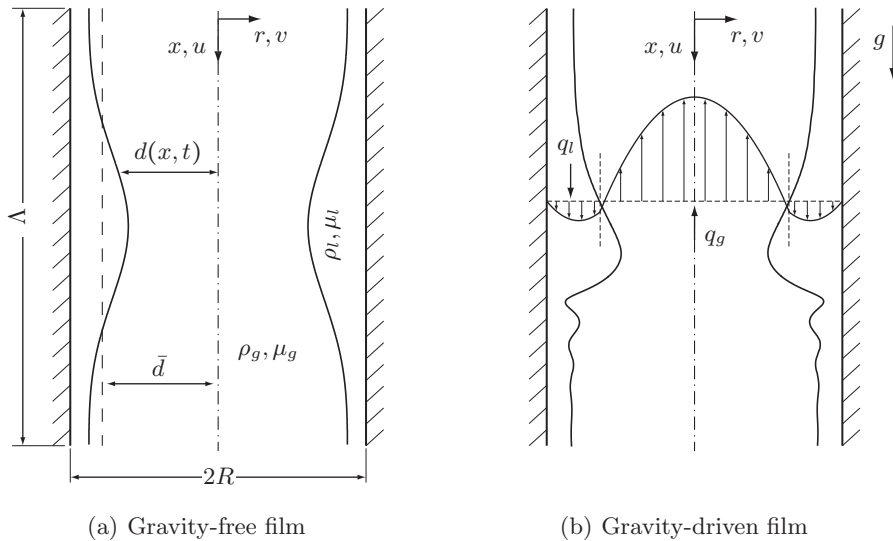


FIGURE 1. Axisymmetric two-phase flows within a narrow cylindrical tube: (a) gravity-free liquid film; (b) gravity-driven liquid film. **Subscript g refers to the active core phase.** The core flow can be either quiescent, co-, or counter-current in both cases (a and b). Although our model is derived for the most general case in section 2, we apply it only to the gravity-free scenario (panel a) in this manuscript (section 3).

40 with a dimensionless cut-off wave number $\alpha=2\pi\bar{d}/\Lambda=1$ (where Λ is the wavelength and
 41 \bar{d} designates the mean core radius, which is exceptionally dimensional here). Beyond this
 42 threshold, the nonlinear evolution of a single-wavelength perturbation leads to one of two
 43 final static configurations, depending on the volume contained in the liquid film (Everett
 44 & Haynes 1972): an unduloid for small liquid volumes, or a liquid bridge for large ones. In
 45 long tubes, where multiple unduloids may form, more complicated dynamics occur due
 46 to interactions between large-amplitude collars and small-amplitude lobes, and the film
 47 may take a very long time to reach a final state (Lister *et al.* 2006). The presence of an
 48 oscillating core flow can also have an effect as it may be tuned to prevent the formation
 49 of liquid bridges (Halpern & Grotberg 2003), occurring when liquid collars grow suffi-
 50 ciently large to occlude the tube cross-section. Predicting these dynamics with sufficient
 51 accuracy at a reasonable computational cost is relevant for two applications: two-phase
 52 flow in porous media (Olbricht 1996) encountered in the process of oil recovery by water
 53 injection; and biological films in human pulmonary capillaries and their interaction with
 54 the respiratory air flow (Grotberg 1994; Heil & Hazel 2011; Grotberg 2011).

55 When axial gravity is added as an external driving force, figure 1(b), the film falls
 56 downward and develops long surface waves due to the convective Kapitza instability
 57 (Kapitza 1948; Brooke Benjamin 1957), which has been studied extensively with respect
 58 to planar falling liquid films (Alekseenko *et al.* 1994; Kalliadasis *et al.* 2012). In our
 59 cylindrical case, these dynamics are modified by the Plateau-Rayleigh instability due to
 60 azimuthal free-surface curvature (Ruyer-Quil *et al.* 2008). This introduces the possibility
 61 of absolute instability, i.e. temporal growth of localized disturbances, which may explain
 62 the occlusion of narrow tubes by wavy falling films (Trifonov 1992; Dao & Balakotaiah
 63 2000). Further, the presence of a core (co- or counter-current) gas flow may alter the
 64 dynamics leading to this flooded state, as has been established for planar films in narrow
 65 channels (Drosos *et al.* 2006; Trifonov 2010*a,b*; Dietze & Ruyer-Quil 2013). Prediction

66 and prevention of flooding is crucial for the efficient design and operation of tubular
67 falling film evaporators used e.g. for milk inspissation (Jebson & Chen 1997).

68 When the main driving force results from an imposed pressure difference, one obtains
69 what is conventionally referred to as core-annular flow (Joseph *et al.* 1997), where both
70 phases are usually co-current (technically, figures 1(a) and 1(b) also depict core-annular
71 flows). Such flows may occur in lubricated pipe-lining (Aul & Olbricht 1990; Joseph
72 *et al.* 1999; Gosh *et al.* 2009) or in human bronchial airways (Camassa *et al.* 2012). They
73 are more complicated than the first two scenarios as interfacial waves can result from
74 two additional instabilities: the long-wave Yih instability due to viscosity stratification
75 (Yih 1967; Hickox 1971) and a short-wave instability of the Tollmien-Schlichting type
76 (Preziosi *et al.* 1989; Hu & Joseph 1989). Moreover, an absolute instability can occur
77 even in the absence of surface tension, e.g. in miscible liquid/liquid systems (Selvam
78 *et al.* 2009; d’Olce *et al.* 2008, 2009). These instability mechanisms lead to nonlinear
79 interfacial deformations that significantly alter the flow field (Newhouse & Pozrikidis
80 1992; Bai *et al.* 1996; Kouris & Tsamopoulos 2001, 2002; Govindarajan & Sahu 2014).

81 In this manuscript, we introduce a low-dimensional model based on the weighted resid-
82 ual integral boundary layer (WRIBL) method (Ruyer-Quil & Manneville 2002; Kalliada-
83 sis *et al.* 2012) that is capable of accurately predicting the linear and nonlinear dynamics
84 of the three above-discussed long-wave instability mechanisms at low computational cost.
85 We derive this model for the most general case (figure 1), ensuring applicability for all
86 three flow scenarios, yet apply it only to the first scenario, i.e. gravity-free liquid films in
87 interaction with an active fluid core, figure 1(a), leaving investigation of the other sce-
88 narios to future work. For reasons that are obvious for applications involving such flows,
89 particular attention is paid to the phenomenon of flooding, when interfacial deformations
90 become so large as to form a liquid bridge occluding the cross-section of the tube.

91 We proceed next with an account of previous modelling work, before discussing the
92 salient/novel features of our model. Regarding the gravity-free configuration in figure
93 1(a), early modelling works considered only the liquid film, assuming a passive core fluid,
94 which is valid e.g. for liquid/gas configurations or liquid/liquid configurations dominated
95 by viscous forces (when the film is significantly more viscous than the core). In this limit,
96 Hammond (1983) derived an evolution equation for the core radius d by applying lubri-
97 cation theory. This amounts to imposing a locally developed flow at all times and thus
98 neglecting inertia and streamwise viscous diffusion altogether. Additionally, Hammond
99 made the assumption of thin films, i.e. $(R - \bar{d}) \ll R$ (where \bar{d} once again is dimensional).
100 The resulting evolution equation enabled first calculations of nonlinear interfacial defor-
101 mations, showing the liquid film to organize into ring-shaped collars separated by thin
102 residual film portions or lobes. However, these calculations could not yield insight into
103 the dynamics once the liquid film grows locally thick whilst the lobes drain into the
104 collars. Nonetheless, calculations on long domains by Lister *et al.* (2006), using the same
105 evolution equation, showed that intricate interactions between several neighbouring lobes
106 and collars occur before that limit is reached and drastically slow the drainage of the
107 liquid film. Viscous dissipation in the very thin lobes is decisive for this behaviour, an
108 observation that we will revisit in section 3.3. By relaxing the thin-film hypothesis in
109 the formulation of the interfacial pressure jump, Gauglitz (1988) obtained an evolution
110 equation that can extend beyond thin films and in principle produce the large-amplitude
111 equilibrium shapes of this problem, i.e. stable unduloids and liquid bridges.

112 A first attempt to account for the effect of an active core fluid was undertaken by
113 Halpern & Grotberg (2003). Their approach represents the liquid film with a similar
114 evolution equation as Gauglitz (1988), while taking into account the tangential stress
115 and axial pressure gradient exerted at the fluid/fluid interface by the core fluid. These

116 coupling quantities are obtained by solving the core flow under the assumption of a
 117 “frozen” film surface. This is valid in the limit of high-frequency core-flow-oscillations
 118 considered by Halpern & Grotberg (2003) as a means to prevent flooding. Comparison
 119 with experiments and direct numerical simulations (DNSs) was subsequently performed
 120 in the passive-core limit (Bian *et al.* 2010; Tai *et al.* 2011). We also note that Halpern
 121 *et al.* (2010) introduced a passive-core lubrication model for visco-elastic liquid films.
 122 Elsewhere, modelling has been undertaken to study the pinch-off of a slender cylindrical
 123 fluid thread surrounded by a second fluid phase. Such works usually assume inertialess
 124 flow (Sierou & Lister 2003) and are obtained by long-wave asymptotic expansion.

125 A shortcoming of the above-described modelling approaches is that they do not account
 126 for inertia, which limits their applicability to viscosity-dominated flows. For the case of
 127 a passive core, Johnson *et al.* (1991) remedied this using an integral approach, without
 128 additionally assuming thin films. By radially integrating the continuity and first-order
 129 long-wave Navier-Stokes equations (prescribing an inviscid velocity profile for inertial
 130 terms and an inertialess profile for viscous terms) across the liquid film, a two-equation
 131 model was obtained. Comparisons with exact linear stability calculations showed good
 132 agreement in the inviscid and inertialess limits, and less good agreement when both inertia
 133 and viscosity are relevant. For the case of a mucus-film/passive-core configuration, the
 134 model was shown to capture the formation of unduloids and liquid bridges in accordance
 135 with the criterion of Everett & Haynes (1972). We note that some works on modelling
 136 the pinch-off of slender fluid threads have also accounted for (weak) inertia (Eggers &
 137 Dupont 1994; Eggers & Villermaux 2008; Wang 2013).

138 Regarding gravity-driven liquid-film/core-fluid configurations, modelling work has pri-
 139 marily focussed on a passive core fluid. Trifonov (1992) applied the (first-order) long-
 140 wave integral boundary layer (IBL) method of Shkadov (1967) to falling films flowing
 141 within cylindrical tubes (and on cylindrical wires). Another approach was applied by
 142 Jensen (2000), who derived evolution equations for different portions of the wavy liq-
 143 uid film. Modelling work accounting for an active core fluid (to our knowledge) has
 144 been very scarce. Only recently, Mehidi & Amatousse (2009) derived a fully-coupled
 145 liquid-film/core-fluid model by applying the WRIBL approach to the case of exclusively
 146 gravity-driven core-annular flow, i.e. in the absence of any axial pressure difference. How-
 147 ever, this work was limited to linear stability calculations. We also note that a number of
 148 works has focussed on the related situation of a liquid film flowing down a cylindrical fibre
 149 in a passive atmosphere (Quéré 1999). For instance, Novbari & Oron (2011, 2009) used
 150 the energy integral method (EIM), akin to the WRIBL method, to derive a first-order
 151 model. Later, Ruyer-Quil *et al.* (2008) and Ruyer-Quil & Kalliadasis (2012) obtained a
 152 second-order WRIBL model and showed that accounting for streamwise viscous diffusion
 153 significantly improves linear and nonlinear predictions. We also note the work of Wray
 154 (2013), who derived a thin-film model for electrolyte films in annular gaps.

155 Regarding pressure-driven core-annular flow, we only briefly mention three modelling
 156 works dealing with thin films, referring the reader to Chen & Joseph (1991) for more
 157 information. Frenkel *et al.* (1987) derived a lubrication model for the case of equal den-
 158 sities and viscosities and showed that the presence of a mean flow could saturate interfacial
 159 waves resulting from the Plateau-Rayleigh instability. Similarly, Papageorgiou *et al.*
 160 (1990) derived a weakly nonlinear model that allows for disparate viscosities in the film
 161 and core. Later, Kerchman (1995) derived a thin-film evolution equation by asymptotic
 162 expansion, while taking into account the interfacial shear stress exerted on the liquid
 163 film by the core flow. Nonlinear simulations using this model were shown to be in good
 164 agreement with experiments by Aul & Olbricht (1990).

165 The model introduced in this manuscript mitigates some of the above-discussed short-

166 comings of previous modelling works. It is obtained by applying the WRIBL approach to
 167 both fluid phases, while fully taking into account inter-phase coupling. In that sense, it is
 168 a cylindrical extension of the planar two-phase model of Dietze & Ruyer-Quil (2013). The
 169 underlying assumptions are that interfacial deformations remain long compared to the
 170 radial extent of the respective phases, which we express in terms of the long-wave param-
 171 eter $\epsilon = R/\Lambda \ll 1$, that the characteristic Reynolds number is moderate in both phases
 172 (inertial effects are moderate), and that the Weber number, relating inertia to capillary
 173 forces, is small (capillary effects are important). Our model is based on a second-order
 174 development in the long-wave parameter ϵ so that inertia, streamwise viscous diffusion
 175 and viscous stresses in the inter-phase coupling conditions are taken into account.

176 In particular, this leads to the following salient/novel features: (a) By design, the model
 177 analytically yields the asymptotic growth rates and wave speeds of long-wave instabilities
 178 in core-annular flow (Hickox 1971). Further, the short-wave linear cut-off wavelength for
 179 the gravity-free scenario (Plateau-Rayleigh instability) is recovered analytically; (b) By
 180 accounting for inertia, the model allows to treat situations that do not satisfy the creeping
 181 flow assumption. For example, we show in section 3.1 that this is the case for liquid-bridge
 182 formation in a gravity-free water/air system. In contrast to lubrication theory models,
 183 our model can accurately predict the time to flooding even in such situations. Further, the
 184 WRIBL approach applies a consistent base velocity profile when integrating the boundary
 185 layer equations, as opposed to Johnson *et al.* (1991), who used different approximations
 186 (inviscid, inertialess) for different terms in the governing equations (inertial, viscous).
 187 This improves the consistency of linear instability predictions when inertial *and* viscous
 188 effects are relevant. We also point out that accounting for inertia is a basic requirement
 189 to capture surface waves in falling liquid films; (c) The model treats both phases equally
 190 and fully accounts for inter-phase coupling, without imposing any restrictions on the
 191 fluid combination. As opposed to passive-core models (Johnson *et al.* 1991; Trifonov
 192 1992), it can thus treat fluid combinations where the film viscosity is not dominant, e.g.
 193 water/silicone-oil. Further, it allows to fully reconstruct the velocity field in both phases
 194 and is not limited to high-frequency core flow oscillations, as opposed to the model by
 195 Halpern & Grotberg (2003); (d) Our model includes an additional equation for the axial
 196 derivative of the interfacial core-fluid pressure, enabling to predict the pressure drop in
 197 the case of imposed flow rate or to impose a driving pressure difference. This allows to
 198 consider different types of driving force. In particular, the three scenarios encompassed by
 199 figure 1 can be recovered, i.e. gravity-free and gravity-driven liquid films in interaction
 200 with an active co- or counter-current core flow and pressure-driven core-annular flows. By
 201 contrast, Mehidi & Amatoousse (2009) assume a zero pressure drop in their model, which
 202 is thus limited to exclusively gravity-driven co-current two-phase flow; (e) Our model
 203 does not assume thin films in relation to the tube radius and can thus predict large-
 204 amplitude interfacial deformations up to the point of flooding, when the cross-section
 205 of the tube is obstructed; (f) By accounting for streamwise viscous diffusion (in both
 206 phases), our model can accurately predict the dynamics of very thin films developing
 207 capillary waves or bulges. For example, we show in section 3.3 that this is essential to
 208 accurately capture the long-time behaviour of thin gravity-free films. Also, it is essential
 209 to describe capillary waves in falling liquid films; (g) Finally, our model allows calculations
 210 at drastically reduced computational cost in comparison to full DNSs.

211 The remainder of the manuscript is structured as follows. We derive our WRIBL model
 212 from first principles in section 2 for the most general case (figure 1), i.e. without distin-
 213 guishing between the scenarios of gravity-free/gravity-driven films and pressure-driven
 214 core-annular flows. Thereby, specific care is taken to write mathematical expressions in

215 a succinct form, in order to allow re-use of the model by others. In section 3, we apply
 216 our model to gravity-free liquid films in interaction with an active fluid core, figure 1(a).
 217 Specific attention is paid to the phenomenon of flooding, which occurs when liquid col-
 218 lars grow sufficiently large to form a liquid bridge occluding the tube cross-section. We
 219 start in subsection 3.1 by validating model calculations with Navier-Stokes calculations of
 220 linear stability and nonlinear two-phase flow dynamics. In subsections 3.2 to 3.4, we then
 221 focus on a number of novel/salient features which we have found for this declaredly well
 222 studied flow scenario thanks to the advantages/improvements contained in our model.
 223 Firstly (section 3.2), we have found that accounting for inertia as well as full coupling
 224 between liquid film and fluid core is essential to accurately predict the flooding dynamics
 225 for fluid pairings that are not dominated by viscosity, e.g. water/air and water/silicone-
 226 oil. Secondly, section 3.3 concerns an interesting phenomenon we have observed in liquid
 227 films that are rather thin, yet too thick to develop an unduloid and must thus eventually
 228 evolve toward a liquid bridge. We have found that this transition is drastically slowed
 229 and effectively halted due to a viscous blocking mechanism that intervenes once the thin
 230 residual film between two liquid collars has buckled. Only at very large times flooding
 231 eventually occurs, when symmetry breaking in the buckled residual film (due to small
 232 perturbations) produces a sliding motion that re-initiates growth of the liquid collars. Im-
 233 portantly, streamwise viscous diffusion is essential to accurately predict this mechanism.
 234 Finally, subsection 3.4 investigates the effect of a low-frequency oscillating core flow, such
 235 as may occur in human pulmonary capillaries. Interestingly, we find that such oscilla-
 236 tions accelerate the above-described sliding-induced flooding mechanism. In subsections
 237 3.3 and 3.4, we also show the occurrence of intricate vorticity-carrying structures in the
 238 two-phase flow. Conclusions are drawn in section 4 and the manuscript is completed by
 239 an appendix succinctly summarizing mathematical expressions intervening in section 2
 240 (appendices A to C) and presenting supplementary validation results (appendix D).

241 2. Model formulation

242 We consider the laminar axisymmetric flow of two immiscible continuous and constant-
 243 property Newtonian fluid phases within a cylindrical tube, as sketched in figure 1. The in-
 244 ner phase of this core-annular flow arrangement is referred to with subscript “ g ”, while the
 245 phase lining the tube wall is indexed with “ l ”. In subsequent sections, we will consider a
 246 specific sub-scenario, i.e. gravity-free liquid films subjected to an active gas or liquid core,
 247 where the relative orientation of the flow rates $\tilde{q}_g = 2\pi \int_0^{\tilde{d}} \tilde{u}_g \tilde{r} d\tilde{r}$ and $\tilde{q}_l = 2\pi \int_{\tilde{d}}^R \tilde{u}_l \tilde{r} d\tilde{r}$
 248 vary. In the current section, we make assumptions neither about this nor about the nature
 249 of the driving force and consider the most general case. We also note that the tilde
 250 symbol is used to distinguish dimensional quantities throughout.

251 2.1. Governing equations truncated in the long-wave limit

252 Our study is focussed on wavy core-annular flows displaying wavelengths much larger
 253 than the radius of the tube, i.e. $\epsilon = R/\Lambda \ll 1$. We invoke this long-wave assumption to
 254 truncate the governing equations at $O(\epsilon^2)$, following Dietze & Ruyer-Quil (2013), who
 255 derived a similar model for two-phase flow through a rectangular channel. From the axial
 256 and radial Navier-Stokes equations, one thus obtains the $O(\epsilon^2)$ -consistent boundary layer
 257 equations for the respective phases, written here in non-dimensional notation ($j = l, g$):

$$258 \operatorname{Re}_j [\partial_t u_j + u_j \partial_x u_j + v_j \partial_r u_j] = -\operatorname{Re}_j \partial_x (p_j|_{r=d}) + \frac{\operatorname{Re}_j}{\operatorname{Fr}^2} + \mathcal{L}(u_j) + 2\partial_{xx} u_j - \partial_x (\partial_x u_j|_{r=d}), \quad (2.1a)$$

where lengths have been non-dimensionalized with the tube radius R , velocities with a characteristic velocity U , pressure with the corresponding dynamic pressure $\rho_j U^2$, and time using R/U . Non-dimensional variables are denoted using regular symbols, i.e. without any attributes, as opposed to dimensional quantities which will be distinguished with a tilde. The dimensionless groups appearing in the above equations are the Reynolds numbers $\text{Re}_j = U R \rho_j / \mu_j$ and the Froude number $Fr = U / (g R)^{1/2}$. We note that the same velocity scale U is chosen for both phases in order to ensure consistent time scales. If the flow rates in the annular and/or core phase are imposed, U may be chosen as one of the superficial velocities, while, in the case of a static film/core arrangement, an internal velocity scale such as obtained by balancing capillary and viscous forces, i.e. $U = \sigma / \mu_l$, may be chosen. In (2.1a), \mathcal{L} refers to the laplacian radial operator in axisymmetric geometries, i.e. $\mathcal{L}(\phi) \equiv \frac{1}{r} \frac{\partial}{\partial r} \left(r \frac{\partial \phi}{\partial r} \right)$. In (2.1a), the free-surface terms $\partial_x (p_j|_{r=d})$ and $\partial_x (\partial_x u_j|_{r=d})$ were substituted for the pressure derivative $\partial_x p_j$ in the axial momentum equation as a result of integrating the radial momentum equation from r to d . Meanwhile, the continuity equation writes:

$$\frac{1}{r} \frac{\partial}{\partial r} (r v_j) + \partial_x u_j = 0. \quad (2.1b)$$

Equations (2.1a) and (2.1b) are completed by the $O(\epsilon^2)$ inter-phase coupling conditions for normal and tangential stresses at $r = d$:

$$\text{Re}_l (p_l - \Pi_\rho p_g) = \text{We}^{-1} \text{Re}_l \kappa + 2 [\partial_r v_l - \partial_x d \partial_r u_l] - 2 \Pi_\mu [\partial_r v_g - \partial_x d \partial_r u_g], \quad (2.1c)$$

$$\partial_r u_l - \Pi_\mu \partial_r u_g = 2 \partial_x d (\partial_x u_l - \partial_r v_l) - \partial_x v_l - \Pi_\mu [2 \partial_x d (\partial_x u_g - \partial_r v_g) - \partial_x v_g], \quad (2.1d)$$

where $\text{We} = (\rho_l R U^2) / \sigma$ is the Weber number (note that, in the literature on falling liquid films, We is written as the inverse of this definition), $\Pi_\mu = \mu_g / \mu_l$ and $\Pi_\rho = \rho_g / \rho_l$ designate the viscosity and density ratios, and κ represents the free-surface curvature truncated at $O(\epsilon^2)$:

$$\kappa = \partial_{xx} d - \frac{1}{d} \left[1 - \frac{1}{2} (\partial_x d)^2 \right], \quad (2.1e)$$

as well as the continuity for the velocity components:

$$u_l|_{r=d} = u_g|_{r=d}, \quad v_l|_{r=d} = v_g|_{r=d}. \quad (2.1f)$$

The system is completed by the no-slip condition at the tube wall and the symmetry condition at the centreline:

$$u_l|_{r=1} = v_l|_{r=1} = 0, \quad \partial_r u_g|_{r=0} = v_g|_{r=0} = 0. \quad (2.1g)$$

2.2. Weighted integral approach

Following Dietze & Ruyer-Quil (2013), we obtain our model equations by weighted integration of (2.1a) across the respective phases. Formally, we introduce the scalar product $\langle A|B \rangle = 2\pi \left(\Pi_\mu \int_0^d A_g B_g r dr + \int_d^1 A_l B_l r dr \right)$, where the choice of a factor Π_μ in front of the integral in the gas phase is a direct consequence of the continuity of tangential stresses (2.1d). Writing the boundary layer equations (2.1a) as BLE_j , we introduce the weight functions $w_j(r)$ and evaluate the residual $\langle BLE|w \rangle$. This will lead to two dynamic model equations derived in the following subsections. In addition, two kinematic equations are obtained by integrating (2.1b) across the respective phases ($j = l, g$):

$$\partial_x q_j - \varepsilon_j 2\pi d \partial_t d = 0, \quad (2.2)$$

where the kinematic condition $v_j|_{r=d} = \partial_t d + u_j|_{r=d} \partial_x d$ was employed and $\varepsilon_l = 1$, $\varepsilon_g = -1$.

2.3. Decomposition of the velocity field

To evaluate $\langle BLE|w \rangle$, we decompose the streamwise velocity component into an $O(1)$ and an $O(\epsilon)$ contribution:

$$u_j(x, r, t) = \underbrace{\hat{u}_j(x, r, t)}_{O(1)} + \underbrace{u_j^{(1)}(x, r, t)}_{O(\epsilon)}. \quad (2.3)$$

The leading order profile $\hat{u}_j(x, r, t)$ satisfies the governing equations (2.1) truncated at $O(1)$ and is additionally required to yield the **local and instantaneous flow rates** in the respective phases, i.e.:

$$q_l = 2\pi \int_d^1 \hat{u}_l r dr, \quad q_g = 2\pi \int_0^d \hat{u}_g r dr, \quad (2.4)$$

which amounts to imposing a gauge condition on the $O(\epsilon)$ corrections $u^{(1)}$:

$$\int_0^d u_g^{(1)} r dr = \int_d^1 u_l^{(1)} r dr = 0. \quad (2.5)$$

This ensures that \hat{u}_j is sufficiently close to the real profile (as evidenced by the flow field comparisons in figures 4, 7(a) and 7(b)) so that the separation of scales (2.3) remains satisfied. It turns out that $\hat{u}_j(x, r, t)$ can then be written as:

$$\hat{u}_j(x, r, t) = q_i(x, t) f_{ij}(r; d), \quad (2.6)$$

where, once again, $j = l, g$ distinguishes the two phases and the explicit dependence on the core radius d is emphasized by the notation $f_{ij}(r; d)$. Also, Einstein's notation has been used so that $q_i(x, t) f_{ij}(r; d)$ is to be read as the sum $q_g(x, t) f_{gj}(r; d) + q_l(x, t) f_{lj}(r; d)$. The formulation in (2.6) will help to derive the model equations in a succinct form. Agreement of the ansatz (2.6) with the base state requires that the functions f_{ij} satisfy:

$$\mathcal{L}(f_{ij}) \equiv \frac{1}{r} \frac{\partial}{\partial r} \left(r \frac{\partial f_{ij}}{\partial r} \right) = C_{ij} \quad (2.7a)$$

with the boundary conditions:

$$\begin{aligned} f_{il}|_{r=d} &= f_{ig}|_{r=d}, & \partial_r f_{il}|_{r=d} &= \Pi_\mu \partial_r f_{ig}|_{r=d}, \\ f_{il}|_{r=1} &= 0, & \text{and } \partial_r f_{ig}|_{r=0} &= 0. \end{aligned} \quad (2.7b)$$

The solutions to this boundary value problem (2.7) are as follows:

$$\begin{aligned} f_{jl}(r; d) &= \frac{C_{jl}}{4} (r^2 - 1) + D_{jl} \ln(r) \text{ with } D_{jl} = \frac{d^2}{2} (\Pi_\mu C_{jg} - C_{jl}), \\ f_{jg}(r; d) &= \frac{C_{jg}}{4} (r^2 - d^2) + f_{jl}(d; d) \text{ with } f_{jl}(d; d) = \frac{1}{4} C_{jl} (d^2 - 1) + D_{jl} \ln(d), \end{aligned} \quad (2.8)$$

wherein the constants C_{ij} are determined by the integral constraints resulting from (2.4):

$$2\pi \int_0^d f_{ig} r dr = \delta_{ig} \quad \text{and} \quad 2\pi \int_d^1 f_{il} r dr = \delta_{il}, \quad (2.9)$$

and δ_{ij} is the usual Kronecker symbol.

The radial velocity component v is computed from the continuity equation (2.1b), using the no-penetration condition at the wall $v_l|_{r=1} = 0$ and the symmetry condition $v_g|_{r=0} = 0$ on the centreline:

$$v_g = -\frac{1}{r} \int_0^r \partial_x u_g r dr \quad \text{and} \quad v_l = -\frac{1}{r} \int_1^r \partial_x u_l r dr. \quad (2.10)$$

315 Later, it will become necessary to compute the derivatives of $\hat{u}(x, r, t)$ with respect to
 316 the core radius d . We introduce a simplified notation of these derivatives here. The first
 317 derivatives $\partial_d f_{ij} = \lim_{\delta d \rightarrow 0} \{(f_{ij}(r; d + \delta d) - f_{ij}(r; d)) / \delta d\}$ are solutions to $\mathcal{L}(\partial_d f_{ij}) =$
 318 $\partial_d C_{ij}$ in addition to verifying the integral constraints:

$$\int_0^d \partial_d f_{ig} r dr + d f_{ig}|_{r=d} = 0, \quad \int_d^1 \partial_d f_{il} r dr - d f_{il}|_{r=d} = 0, \quad (2.11)$$

319 the boundary conditions (2.7b) derived with respect to d , and the coupling conditions at
 320 the free surface ($r = d$):

$$\partial_d f_{il} + \partial_r f_{il} = \partial_d f_{ig} + \partial_r f_{ig}, \quad \partial_{dr} f_{il} + \partial_{rr} f_{il} = \Pi_\mu [\partial_{dr} f_{ig} + \partial_{rr} f_{ig}]. \quad (2.12)$$

321 Since $\partial_d f_{ij}$ and f_{ij} **satisfy similar linear boundary value problems**, they can be expressed
 322 as a linear combination of one another:

$$\partial_d f_{ij} = a_{ijk} f_{kj}, \quad (2.13)$$

323 wherein the coefficients a_{ijk} are functions of $f_{il}|_{r=d}$ and $\partial_r f_{il}|_{r=d}$ exceptionally denoted
 324 f_{il} and $\partial_r f_{il}$ here:

$$a_{iil} = 2\pi f_{il} d, \quad (2.14)$$

$$a_{igl} = a_{iil} + \frac{\Pi_\mu f_{gl} [-C_{il} + \Pi_\mu C_{ig}] + \partial_r f_{gl} (\Pi_\mu - 1) \partial_r f_{il}}{\Pi_\mu D}, \quad (2.15)$$

$$a_{igg} = -2\pi f_{il} d, \quad (2.16)$$

$$a_{ilg} = a_{igg} + \frac{\Pi_\mu f_{il} [-C_{il} + \Pi_\mu C_{ig}] + \partial_r f_{il} (\Pi_\mu - 1) \partial_r f_{il}}{\Pi_\mu D}, \quad (2.17)$$

$$D = f_{il} \partial_r f_{gl} - f_{gl} \partial_r f_{il}. \quad (2.18)$$

325 With the above notations, the radial velocity component can be written as follows:

$$v_j = -\frac{1}{r} [a_{ijk} q_i \partial_x d l_{kj}(r; d) + \partial_x q_i l_{ij}(r; d)] + O(\epsilon), \quad (2.19)$$

326 where:

$$\begin{aligned} l_{ig}(r; d) &\equiv \int_0^r f_{ig} r dr \\ &= \frac{r^2}{96} \left\{ C_{ig}^2 r^4 - 3C_{ig} r^2 (C_{ig} d^2 - 4f_{il}(d; d)) + 3(C_{ig} d^2 - 4f_{il}(d; d))^2 \right\}, \end{aligned} \quad (2.20)$$

$$\begin{aligned} l_{il}(r; d) &\equiv \int_1^r f_{il} r dr \\ &= \frac{1}{96} \left\{ (r^2 - 1^2) [C_{il}^2 (r^2 - 1^2)^2 - 3C_{il} D_{il} (r^2 - 31^2) + 24D_{il}^2] \right. \\ &\quad \left. + 12D_{il} r^2 \ln(r) [C_{il} (r^2 - 2) + 4D_{il} \ln(r)] \right\}. \end{aligned} \quad (2.21)$$

327 Similarly to the first derivatives, the second derivatives satisfy $\partial_{dd} f_{ij} = b_{ijk} f_{kj}$, where the
 328 coefficients b_{ijk} are again functions of $f_{il}|_{r=d}$ and $\partial_r f_{il}|_{r=d}$, once again denoted f_{il} and

329 $\partial_r f_{il}$ here for simplicity::

$$b_{iil} = -2\pi [f_{il} + d(\partial_d f_{il} + \partial_r f_{il})], \quad (2.22)$$

$$b_{igl} = b_{iil} + (Dd)^{-1} \{f_{gl} [-C_{il} - 2d\partial_d C_{il} + \Pi_\mu C_{ig} + 2\Pi_\mu d\partial_d C_{ig}] \\ + \partial_r f_{gl} [d(C_{il} - C_{ig}) - \partial_d f_{ig} + \partial_d f_{il} + 2d(\partial_{dr} f_{il} - \partial_{dr} f_{ig})]\}, \quad (2.23)$$

$$b_{ilg} = b_{igg} + (Dd)^{-1} \{f_{il} [-C_{il} - 2d\partial_d C_{il} + \Pi_\mu C_{ig} + 2\Pi_\mu d\partial_d C_{ig}] \\ + \partial_r f_{il} [d(C_{il} - C_{ig}) - \partial_d f_{ig} + \partial_d f_{il} + 2d(\partial_{dr} f_{il} - \partial_{dr} f_{ig})]\}, \quad (2.24)$$

$$b_{igg} = -2\pi [f_{ig} + d(\partial_d f_{ig} + \partial_r f_{ig})]. \quad (2.25)$$

330 2.4. Choice of weight functions w_j and elimination of velocity corrections $u_j^{(1)}$

331 For the much simpler case of a liquid film in a passive atmosphere, Ruyer-Quil *et al.*
332 (2014) showed that, substituting (2.3) for u_j in the governing equations, the correc-
333 tion fields $u_j^{(1)}$ could be solved recursively as a series in ϵ . In our case, this would have
334 the form $\sum_k \epsilon^k u_{jk}^{(1)}(q_j, d, \partial_x p_j|_{r=d}, r)$ and the gauge conditions (2.5) would yield two dy-
335 namic model equations coupling core radius, flow rates and pressure gradients (related by
336 2.1c). However, this approach would involve cumbersome algebra. The weighted residual
337 method on the other hand offers a welcome short-cut to determine the looked-after model
338 equations. In this method, the weights are adjusted so as to cancel the contributions of
339 the corrections $u_j^{(1)}$ in the computation of the residuals, as detailed below.

340 We consider flows of moderate Reynolds number and thus neglect $O(Re_j \epsilon^2)$ inertial
341 terms in $\langle BLE|w \rangle$. Then, the only remaining expression containing the unknown velocity
342 corrections $u_j^{(1)}$ is $\langle \mathcal{L}u|w \rangle$, which is of $O(1)$. By imposing the same boundary and coupling
343 conditions on the weight functions w_j than on the leading order velocity profile \hat{u}_j :

$$w_l|_{r=d} = w_g|_{r=d}, \quad \partial_r w_l|_{r=d} = \Pi_\mu \partial_r w_l|_{r=d}, \quad w_l|_{r=1} = 0, \quad \partial_r w_g|_{r=0} = 0, \quad (2.26)$$

344 this expression can be recast by two integrations by parts:

$$\langle \mathcal{L}u|w \rangle = -2\pi d w_j|_{r=d} (\partial_r u_l - \Pi_\mu \partial_r u_g)|_{r=d} + \langle u|\mathcal{L}w \rangle, \quad (2.27)$$

345 where the stress jump $(\partial_r u_l - \Pi_\mu \partial_r u_g)|_{r=d}$, given by the tangential stress balance (2.1d),
346 is of $O(\epsilon^2)$ and terms containing the first-order corrections $u_j^{(1)}$ thus drop out. Notice
347 that (2.27) implies that the linear operator \mathcal{L} is self-adjoint in the space of functions
348 verifying (2.26) and equipped with the scalar product $\langle A|B \rangle$. The gauge condition (2.5)
349 can then be used to cancel out the remaining first-order corrections $\langle u^{(1)}|\mathcal{L}w \rangle$ by choosing
350 w_j solution to:

$$\mathcal{L}w_j = C_j. \quad (2.28)$$

351 As a result, our model can account for crosswise viscous diffusion in a manner consistent
352 with the $O(\epsilon^2)$ long-wave approximation. To uniquely define the weight functions, the
353 constants C_j remain to be specified. By choosing different sets of values for these, we
354 derive two dynamic model equations. The first is obtained by requiring:

$$\int_0^d w_g r dr = - \int_d^1 w_l r dr, \quad (2.29)$$

355 which allows to recast the pressure terms appearing in the residual $\langle BLE|w \rangle$:

$$\langle -\text{Re} \partial_x (p|_{r=d})|w \rangle = \text{Re} \partial_x (p_l|_{r=d} - \Pi_\rho p_g|_{r=d}) 2\pi \int_0^d w_g r dr, \quad (2.30)$$

356 where we have used the equality $\Pi_\mu \text{Re}_g = \Pi_\rho \text{Re}_l$ in the algebra. The pressure jump

357 $\text{Re}_l (p_l|_{r=d} - \Pi_\rho p_g|_{r=d})$ is given by (2.1c) so that the choice (2.29) effectively eliminates the
 358 pressure variable from the system of equations. A suitable choice of the weight functions,
 359 i.e. satisfying (2.28), (2.26) and (2.29), then is:

$$w_j(r; d) = f_{lj}(r; d) - f_{gj}(r; d), \quad (2.31)$$

360 where the subscript $j = g, l$ once again refers either to the liquid or the gas phase. With
 361 this choice, $2\pi \int_0^d w_g r dr = -1$ and $2\pi \int_d^1 w_l r dr = 1$.

362 Alternatively, by setting:

$$w_j^*(r; d) = f_{lj}(r; d) + f_{gj}(r; d), \quad (2.32)$$

363 and using (2.1c) to replace $\partial_x p_l|_{r=d}$ in $\langle BLE|w^* \rangle$, we obtain an equation for the gas-side
 364 free-surface pressure $p_g|_{r=d}$. The star symbol is employed here to denote the weight func-
 365 tions used to obtain this second dynamic model equation and $2\pi \int_0^d w_g^* r dr = 2\pi \int_d^1 w_l^* r dr =$
 366 1.

2.5. Final model equations

367 The system of four unknowns d , q_l , q_g and $p_g|_{r=d}$ is governed by the two kinematic
 368 equations (2.2) as well as two dynamic equations. The first is obtained from $\langle BLE|w \rangle$,
 369 using the weight functions defined in (2.31):

$$\begin{aligned} \text{Re}_l \{ S_i \partial_t q_i + F_{ij} q_i \partial_x q_j + G_{ij} q_i q_j \partial_x d \} &= \text{Re}_l \text{Fr}^{-2} (1 - \Pi_\rho) \\ &- \text{We}^{-1} \text{Re}_l \partial_x [\kappa] + (C_{jl} - \Pi_\mu C_{jg}) q_j \\ &+ J_j q_j (\partial_x d)^2 + K_j \partial_x q_j \partial_x d + L_j q_j \partial_{xx} d + M_j \partial_{xx} q_j. \end{aligned} \quad (2.33)$$

371 All coefficients therein are functions of d and are written out in appendix A. The second
 372 is obtained from $\langle BLE|w^* \rangle$, using the weight functions defined in (2.32):

$$\begin{aligned} 2\Pi_\rho \text{Re}_l \partial_x p_g|_{r=d} &= -\text{Re}_l \{ S_i^* \partial_t q_i + F_{ij}^* q_i \partial_x q_j + G_{ij}^* q_i q_j \partial_x d \} \\ &+ \text{Re}_l \text{Fr}^{-2} (1 + \Pi_\rho) - \text{We}^{-1} \text{Re}_l \partial_x [\kappa] + (C_{jl} + \Pi_\mu C_{jg}) q_j \\ &+ J_j^* q_j (\partial_x d)^2 + K_j^* \partial_x q_j \partial_x d + L_j^* q_j \partial_{xx} d + M_j^* \partial_{xx} q_j. \end{aligned} \quad (2.34)$$

373 and the coefficients for this equation (denoted with a star) are written out in appendix B.
 374 A much more succinct formulation of the model coefficients than in Dietze & Ruyer-Quil
 375 (2013) was achieved as a result of the chosen parametrization of the leading-order velocity
 376 profile (2.6). **We note that the relation $\Pi_\mu \text{Re}_g = \Pi_\rho \text{Re}_l$ was employed once-again to write**
 377 **the above equations in terms of the film Reynolds number Re_l only, thus simplifying the**
 378 **algebra. We also remind the reader that the weighted residual technique enabled us to**
 379 **obtain (2.33) and (2.34) without having to determine the correction fields $u_j^{(1)}$, which**
 380 **considerably reduces the necessary algebra.**

381 Equations (2.33) and (2.34) as well as the coefficients contained therein were obtained
 382 independently and identically by the two authors of this manuscript. A further test
 383 against derivation errors was performed by verifying that our model analytically recovers
 384 the stability results of Hickox (1971) for axisymmetric core-annular flow in the limit of
 385 infinitely long waves, i.e. $\epsilon \rightarrow 0$. **Also, the model analytically predicts the short-wave**
 386 **cut-off for the Plateau-Rayleigh instability in gravity-free liquid films. This follows from**
 387 **retaining the second axial derivative $\partial_{xx} d$ in the formulation of the free-surface curvature**
 388 **(2.1e), as shown e.g. by Eggers & Dupont (1994) and Timmermans & Lister (2002). This**
 389 **term and the azimuthal term are the only ones subsisting in the linear limit of the**
 390 **perturbation curvature. It is of second order in the long-wave parameter ϵ (bearing in**
 391 **mind the assumption $\epsilon \text{We}^{-1} = O(1)$, which we have made throughout). As our model**
 392 **retains second-order terms in the truncated governing equations (with the exception of**

inertial corrections, i.e. terms of type $\epsilon \text{Re}_l u'$, the stabilizing effect of axial free-surface curvature is thus automatically taken into account in the truncated inter-phase normal stress balance (2.1c).

It is also interesting to check our equations in the limit of thin films, i.e. $1 - d \ll 1$, to see if they converge to the evolution equation (3.44) in Hammond (1983). For this, we must consider our equation (2.33) in the passive core ($\Pi_\rho, \Pi_\mu = 0$), gravity-free ($1/Fr=0$), and inertialess ($S_i=F_{ij}=G_{ij}=0$) limits and exclude terms linked to streamwise viscous diffusion ($J_j=K_j=L_j=M_j=0$). This reduces the RHS of (2.33) to the second (capillarity) and third (crosswise viscous diffusion) terms. Now, to obtain a single evolution equation from our two-equation model, (2.33) is differentiated once with respect to x and inserted into (2.2). We then substitute $d = 1 - \delta H$ (using R as the length scale), where H is the dimensionless film thickness, and consider the thin film limit by developing the resulting equation in a Taylor series around $\delta = 0$ in terms of the small parameter $\delta \ll 1$. Truncating this series at fourth order (orders 0 through 3 yield no spatial derivatives) yields Hammond's equation exactly, if the appropriate scaling is chosen. Indeed, setting the velocity scale $U = \sigma/\mu_l$, the coefficient $\text{We}^{-1} \text{Re}_l=1$ and we finally obtain:

$$\partial_t H = -\frac{1}{3} \partial_x [H^3 (\partial_{xxx} H + \partial_x H)]. \quad (2.35)$$

We continue with a few technical remarks regarding our system of model equations. Equations (2.2) and (2.33) represent a closed system, fully describing the flow in terms of the kinematic unknowns d , q_l and q_g , for which appropriate boundary and initial conditions need to be specified in order to simulate a particular flow situation. In the case of an open calculation domain, flow conditions are uniquely defined by the in- and outlet conditions for the film thickness and respective flow rates. In the case of a closed calculation domain (periodic boundary conditions), integral conditions on two of these three variables need to be specified in order to fix a particular solution. For instance, the mean flow rates \bar{q}_l and \bar{q}_g or the mean core radius \bar{d} and \bar{q}_g (or \bar{q}_l) can be prescribed. In such cases, equation (2.34) does not directly enter the solution procedure, but can be employed to calculate the core pressure distribution $p_g|_{r=d}$ a posteriori. Alternatively, (2.34) can be integrated over the length of the computational domain in order to obtain an integral relation between the axial core-pressure-drop and the kinematic unknowns. This relation can then be used to prescribe the pressure drop instead of the mean flow rate \bar{q}_g . In this sense, the pressure equation (2.34) is an adjoined equation. In some studies (Mehidi & Amatousse 2009), the total flow rate $q_{\text{tot}}(t) = q_l + q_g$ is introduced instead of the core flow rate q_g . This is a matter of preference and has no particular advantage.

We conclude by contrasting our WRIBL method with the classical asymptotic expansion approach often applied to flows with long-wave instabilities. Classical asymptotic expansion necessarily yields an evolution equation for the position of the interface d . This is a consequence of the fact that, in the long-wave limit, the stability of the base flow admits only one zero eigenvalue corresponding to a uniform displacement of the interface. As a result, the velocity field is completely enslaved to the dynamics of d . The location of the interface is thus the sole degree of freedom retained by the long-wave theory. Said otherwise, the long wave theory assumes the dynamics of the flow to be subordinated to the kinematics of the interface. Consequently, long-wave models may exhibit problematic behaviour when inertia effects become more significant. This has been shown e.g. for falling films, where finite-time blow-up has been observed (Pumir *et al.* 1983). The WRIBL approach introduces secondary degrees of freedom, the flow rates, and thus relaxes the slaving of the velocity field to the free-surface deformations. Consequently, it remains treatable further into the nonlinear regime. This advantage may be

$$\frac{\Lambda}{R} \quad \bar{d} = \frac{R}{\Lambda} \int_0^{\Lambda/R} dx \quad \hat{d}_0 = d_{\max}|_{t=0} - \bar{d} \quad \Pi_\rho = \frac{\rho_g}{\rho_l} \quad \Pi_\mu = \frac{\mu_g}{\mu_l} \quad \text{La} = \frac{\sigma \rho_l R}{\mu_l^2}$$

TABLE 1. Dimensionless parameters varied in section 3 (scales: $U = \sigma/\mu_l$; $L = R$).

less clear for other scenarios, as inertia (which introduces the high-order nonlinearities) does not play the same role e.g. for static films than for falling films. However, as we will see later, figure 8 shows that inertia may also significantly affect the nonlinear dynamics of static films. In any case, deriving a second-order asymptotic model to compare with our WRIBL approach is an interesting suggestion for future work.

3. Results and discussion: gravity-free films with an active fluid core

We demonstrate the capabilities of our WRIBL model by applying it in this section to one of the scenarios encompassed by figure 1. We consider figure 1(a), i.e. gravity-free liquid films in interaction with an active fluid core that is either quiescent (subsections 3.1 to 3.3) or oscillating in time (subsection 3.4). Investigation of other scenarios is left to future work. We remind that, where dimensional quantities are necessary, they will be denoted with a tilde symbol.

3.1. Validation with Navier-Stokes calculations: linear stability, nonlinear surface deformations and two-phase flow dynamics

We consider the flow scenario depicted in figure 1(a), i.e. a gravity-free liquid film lining the inner wall of a cylindrical tube and surrounding a fluid core. In this case, there is no external velocity scale so that we construct $U = \sigma/\mu_l$ by balancing viscous and capillary stresses, while we choose $L = R$ as the length scale. These scales are used throughout the section unless otherwise indicated. The resulting dimensionless groups are the density and viscosity ratios Π_ρ and Π_μ , the dimensionless mean core radius \bar{d} , wavelength Λ/R , and initial perturbation $\hat{d}_0 = d_{\max}|_{t=0} - \bar{d}$ (3.2), while the inverse Weber number We^{-1} , using the internal velocity scale U , takes the form $\text{Oh}^{-2} = \text{La} = \sigma \rho_l R / \mu_l^2$. The dimensionless group $\text{Oh} = \mu_l / \sqrt{\sigma \rho_l R}$ was introduced by von Ohnesorge (von Ohnesorge 1936; McKinley & Renardy 2011) and combines inertia, capillary, and viscous forces. However, for ease of comparing conditions with other works, we will use the Laplace number $\text{La} = \text{Oh}^{-2}$ in the remainder of the manuscript (see table 1). A seventh group intervenes when a pressure difference Δp is applied over the tube, but for now we consider $\Delta p = 0$.

We recall that the considered configuration is unstable to the Plateau-Rayleigh mechanism for $\Lambda/R > 2\pi\bar{d}$ or, in terms of the dimensionless wave number α , $\alpha\bar{d} < 1$ (Rayleigh 1892). This can be seen in figure 2, depicting temporal growth rates from linear stability analysis for different parameter configurations (which we will investigate in more detail in this section). Figure 2 shows that our model passes the most basic test, i.e. it accurately predicts the “exact” linear growth rates obtained from the Orr-Sommerfeld problem. In addition to the non-dimensional growth rate in figure 2(a), we have plotted the dimensional one in 2(b) in order to clarify which configuration is the most unstable, as the dimensionless representation is misleading in this respect. Incidentally, it is interesting to note that, although viscous liquids are considered, the most dangerous wave number α_{\max} corresponds quite closely to the inviscid prediction $\alpha_{\max}\bar{d} = 2^{-1/2}$ (Rayleigh 1892).

Perturbations of wave number $\alpha\bar{d} < 1$ may cause an initially smooth liquid film of radius \bar{d} to transition toward two distinct deformed equilibrium shapes of constant

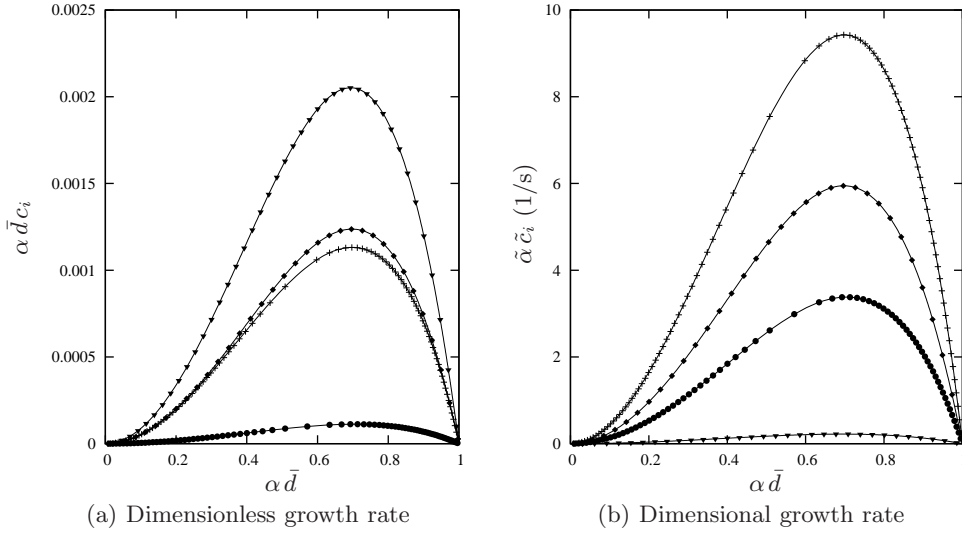


FIGURE 2. Dispersion curves from temporal linear stability analysis. Lines: Orr-Sommerfeld solution; symbols: our model. Gravity-free films in tubes under zero pressure drop for conditions from published work (velocity/length scales: $U=\sigma/\mu_i$; $L=R$). Flow parameters are listed as $[\bar{d}, \text{La} = \sigma \rho_l R/\mu_i^2, \Pi_\rho, \Pi_\mu]$ (see also table 2). \bullet , fig. 5(a) Johnson *et al.* (1991): $[0.9, 21424, \approx 0, \approx 0]$; $+$, fig. 5(b) Johnson *et al.* (1991): $[0.8, 5287, \approx 0, \approx 0]$; \blacklozenge , fig 4(b) Tai *et al.* (2011): $[0.8, 125, \approx 0, \approx 0]$; \blacktriangledown , fig. 7(b) Tai *et al.* (2011): $[0.77, 0.056, 0.95, 0.01]$.

Figures	$\rho_l(\text{kg/m}^3)$	$\rho_g(\text{kg/m}^3)$	$\mu_l(\text{Pas})$	$\mu_g(\text{Pas})$	$\sigma(\text{N/m})$	$R(\text{mm})$	\bar{d}	Λ/R
2, 3(a,b)	1098.3	1.2	$3.1 \cdot 10^{-3}$	$1.8 \cdot 10^{-5}$	0.127	1.5	0.9	6
2, 3(c,d)	1098.3	1.2	$3.1 \cdot 10^{-3}$	$1.8 \cdot 10^{-5}$	0.031	1.5	0.8	6
2	1000	1.2	0.013	$1.8 \cdot 10^{-5}$	0.033	0.027	0.8	-
2, 6(a)	1251	1191	0.624	$\mu_l/100$	0.030	0.58	0.77	7

TABLE 2. Parameters from different works used to validate our model. The first two cases correspond to figure 5 in Johnson *et al.* (1991), who considered a passive core (we use air instead) and specified only dimensionless numbers (we have chosen R , μ_l and ρ_l as free parameters, assigning plausible values). The last two cases correspond to figures 4(b) and 7(b) in Tai *et al.* (2011). Where necessary, Λ/R was rounded to the nearest integer to facilitate DNSs with Gerris.

interfacial curvature (Everett & Haynes 1972): (i) If the dimensionless liquid volume $V_l = \tilde{V}_l/(\pi R^3) = (1 - \bar{d}^2)\Lambda/R$ is small, the liquid forms a so-called unduloid (Delaunay 1841). The axial core radius profile $d(x)$ of this shape is drawn by the focus of an ellipse with major axis R rolled on the tube axis. (ii) If $V_l > 1.73$, the film forms a liquid bridge, flooding the tube and separating two spherical bubbles (or drops) of the core fluid. The threshold value of $V_l = 1.73$ corresponds to the maximal volume an unduloid can attain and is defined in terms of elliptical integrals in Everett & Haynes (1972). Interestingly and in anticipation of our results, **we have found that in thin films** which are too thick to form an unduloid ($V_l > 1.73$), flooding may be significantly delayed (and effectively prevented) due to a buckling mechanism that drastically slows down drainage of the liquid film.

Accurate prediction of flooded states and temporal evolution thitherto is relevant for

492 pulmonary flows in medical science (Grotberg 1994, 2011) and water-aided oil recovery
 493 from porous rock (Olbricht 1996). In what follows, we will scrutinize the predictive capa-
 494 bilities of our model in this respect for a variety of fluid combinations. We point out that,
 495 in contrast to previous modelling work (Johnson *et al.* 1991; Halpern & Grotberg 2003;
 496 Lister *et al.* 2006; Halpern *et al.* 2010), our model takes into account inertia and stream-
 497 wise viscous diffusion in both phases as well as the full inter-phase coupling conditions.
 498 We will show that these effects are indeed relevant for several realistic fluid pairings.

499 Figure 3 compares our model predictions for two cases studied by Johnson *et al.* (1991)
 500 (film of mucus liquid in a passive atmosphere) with our own DNSs using the VOF solver
 501 Gerris (Popinet 2009). Therein, the time scale τ was introduced by Johnson *et al.* (1991)
 502 and is based on an inertialess approximation of the linear temporal growth rate:

$$\tau = 6 \frac{\mu_l R \bar{d}}{\sigma} \left[\alpha^{*4} (1/\alpha^{*2} - 1) (1/\bar{d} - 1)^2 (1/\bar{d}^2 - 1) \right]^{-1}, \quad \alpha^* = \alpha \bar{d} = \frac{2\pi \bar{d}}{\Lambda/R}. \quad (3.1)$$

503 For the top figures 3(a) and 3(b), the liquid volume $V_l < 1.73$, and indeed both the model
 504 and DNS predict the film to evolve toward an unduloid. This is particularly evident in
 505 subfigure 3(b), showing degressive time traces of the minimal and maximal core radii.
 506 In subfigures 3(c) and 3(d), $V_l > 1.73$, and the film evolves toward a liquid bridge as
 507 evidenced by the progressive core radii time traces. Overall, agreement in figure 3 between
 508 DNS and our model is good. In particular, the evolution of the shape of the film surface
 509 (panels a and c) is well predicted. However, the time to flooding (panel d) is slightly
 510 underestimated by the model (7 % error). This results from the fact that, with increasing
 511 amplitude, the long-wave approximation $\Lambda \gg (1 - d)$ is less well fulfilled, explaining why
 512 the deviation between model and DNS data gradually increases over time. **Meanwhile,**
 513 **figures 3(e) and 3(f) show a logarithmic representation of the temporal growth of liquid-**
 514 **collar-amplitudes (following Pozrikidis (1999)) based on the data in figures 3(a) and 3(c),**
 515 **respectively. These time traces (solid lines) are compared to a linear growth scenario**
 516 **(dash-dotted lines) based on the temporal growth rate from linear stability analysis (see**
 517 **figure 2). Both lines coincide in the early stages, when the perturbation amplitude is**
 518 **small and growth is governed by linearized mechanics in the vicinity of the base state.**
 519 **At the time point where both curves start to diverge significantly, these linear mechanics**
 520 **no longer hold and a nonlinear description of the film dynamics is necessary. Here, the**
 521 **advantage of the additional complexity of our nonlinear model becomes apparent. Indeed,**
 522 **comparison of figures 3(e) and 3(f) with figures 3(b) and 3(c) shows that the model yields**
 523 **accurate predictions quite far into the nonlinear growth regime.**

524 Regarding the superposition of model and DNS data in figure 3 and in all subsequent
 525 similar figures, a clarification is required. **Both simulations were initiated with a sinusoidal**
 526 **perturbation of the core radius d at time $t = 0$:**

$$d|_{t=0} = \bar{d} + \hat{d}_0 \sin(2\pi \bar{x}/\Lambda). \quad (3.2)$$

527 However, the initial perturbation amplitude \hat{d}_0 was chosen differently. To limit the
 528 calculation time of our DNSs, we imposed a relatively large initial perturbation in these,
 529 while our model simulations were initiated with a very small excitation amplitude \hat{d}_0 in
 530 order to represent the “entire” time-evolution of the flow. In order to compare both time
 531 traces, the DNS data were shifted until matching the model values of the core radii at
 532 the first DNS data point. This procedure is only applicable in a time range wherein the
 533 interface shape remains close to sinusoidal, which is the case here. We have checked that
 534 changing the initial perturbation amplitude \hat{d}_0 of the model calculation to the value of
 535 the corresponding DNS produces almost exactly (error <1 %) the same time traces from
 536 there onwards.

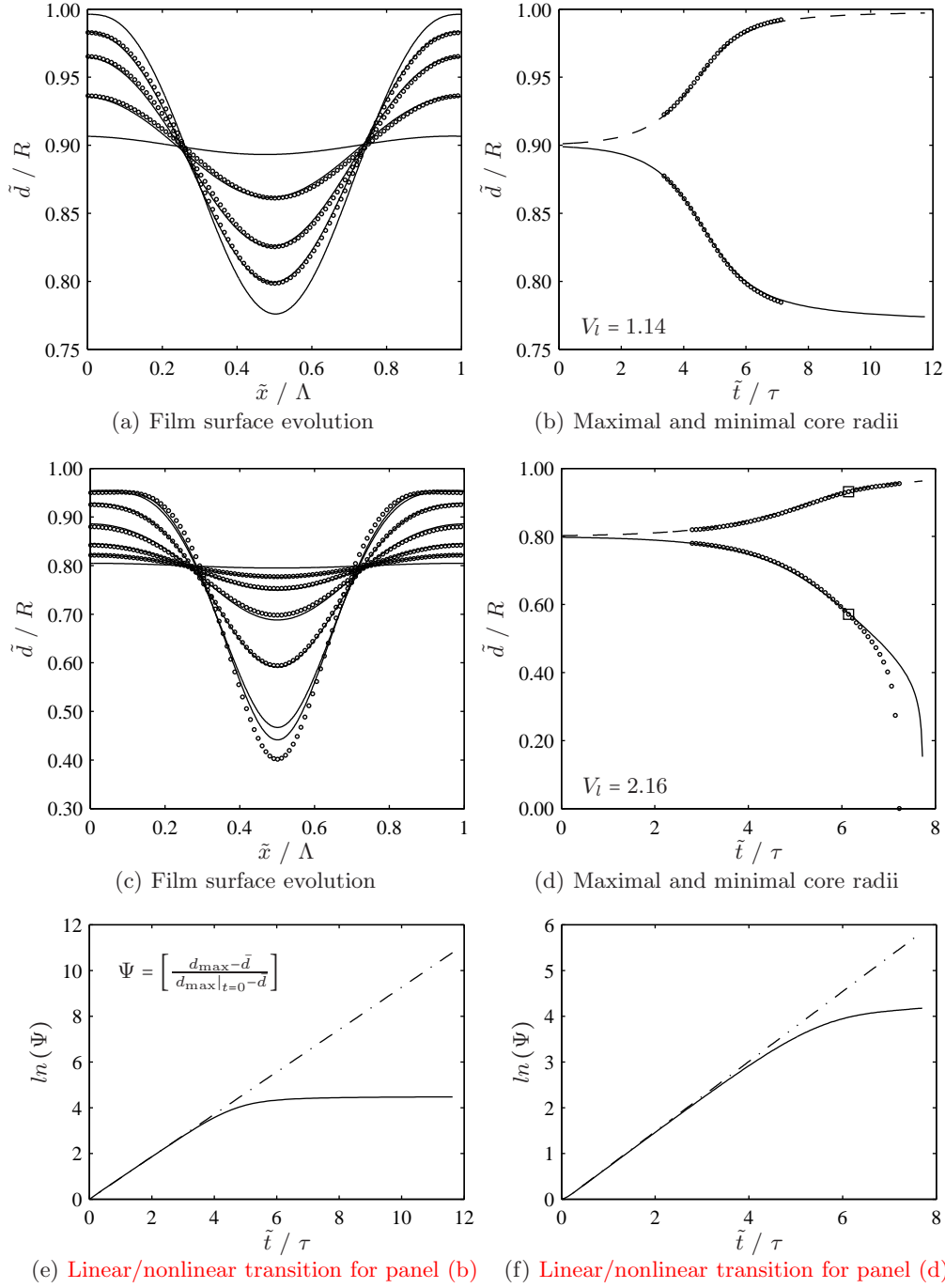


FIGURE 3. Time evolution of annular mucus films in contact with an air core. Parameters correspond to figure 5 in Johnson *et al.* (1991). Panels (a,b): formation of a stable unduloid ($\bar{d} = 0.9$, $\Lambda/R = 6$, $\text{La} = 2.13 \cdot 10^4$, $\bar{d}_0 = d_{\max}|_{t=0} - \bar{d} = 0.001$); panels (c,d): formation of a liquid bridge ($\bar{d} = 0.8$, $\Lambda/R = 6$, $\text{La} = 5.29 \cdot 10^3$, $\bar{d}_0 = 0.0025$). Profiles are displayed at $\tilde{t}/\tau = 2, 4, 5, 6, 10$ (panel a) and $\tilde{t}/\tau = 1, 3, 4, 5, 6, 7, 7.1$ (panel c) respectively with τ according to (3.1) and $\text{La} = (\sigma R \rho_l) / \mu_l^2$. Circles indicate DNS data obtained with the VOF code Gerris (only available time points are shown in panels a and c). Squares highlight the time point displayed in figure 4. **Panels (e,f): logarithmic representation of the linear (dash-dotted line, obtained from stability analysis) and actual (solid line, obtained from model) growth of interfacial perturbations in panels (b,d).**

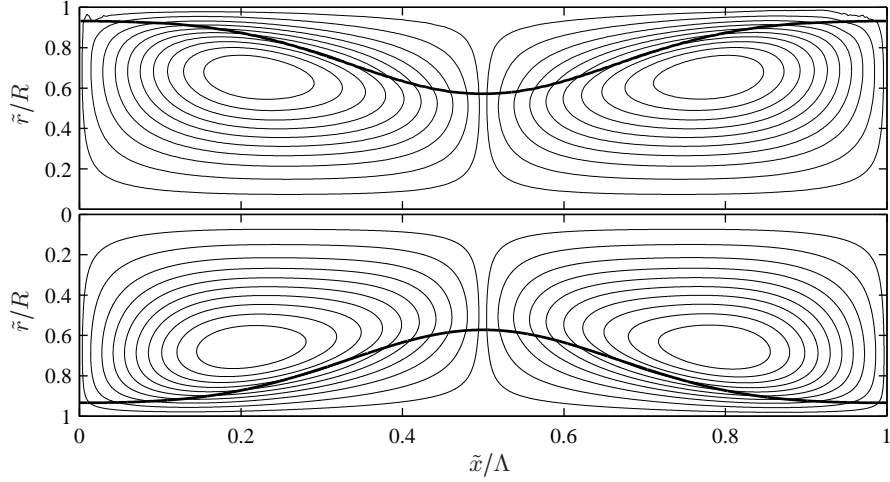


FIGURE 4. Streamlines in the wall-fixed reference frame obtained from DNS (top) and the WRIBL model (bottom). Mucus-film/air-core combination. See figure 3(d) and table 2 for flow conditions and time point (squares in panel 3(d): $\tilde{t}/\tau=6.1$). Stream functions are normalized by their maximum and contour line values are identical in both plots, i.e. $\pm[0.025,0.1:0.1:0.9]$.

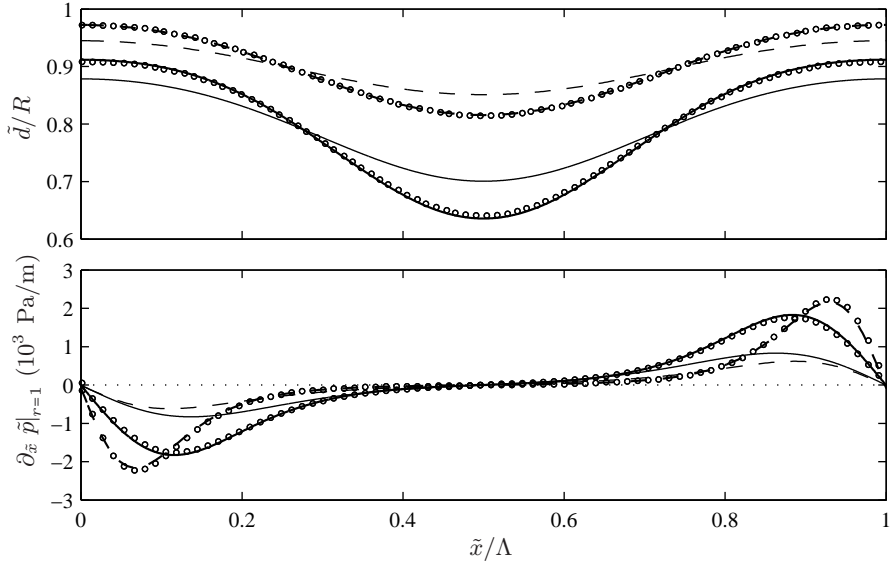


FIGURE 5. Profiles of the axial wall pressure derivative (bottom) and corresponding core radius distribution (top) for the conditions in figures 3(b) (unduloid scenario: $\tilde{t}/\tau=5.4$, thick dashed lines) and 3(d) (liquid bridge scenario: $\tilde{t}/\tau=5.6$, thick solid lines), respectively. Circles mark DNS data and lines model predictions. Thin lines refer to an earlier time point in each case and are not compared to DNS data to avoid cluttering the graph.

537 Figure 4 compares the streamlines computed from our model to DNS data for the
 538 time point highlighted with a square in subfigure 3(d). We point out that, in contrast to
 539 Johnson *et al.* (1991), we did not consider a perfectly passive core phase but instead used
 540 air in both the model and direct simulations. Indeed, in contrast to previous modelling
 541 works, our full account of both fluid phases allows us to obtain the streamlines also in the

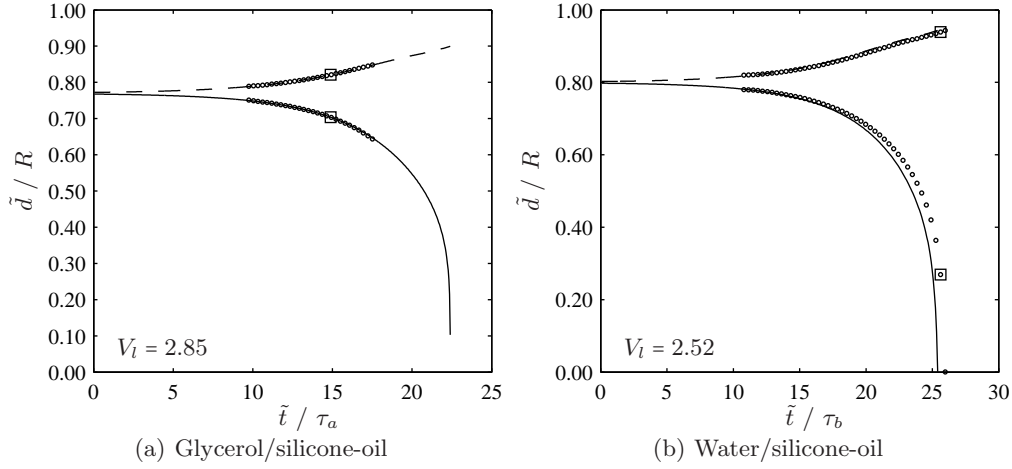


FIGURE 6. Time traces of the minimal and maximal core radii obtained from our model (lines) and DNSs (symbols) for two liquid/liquid configurations reported by Tai *et al.* (2011) and Piroird *et al.* (2011), respectively. (a) $\text{La} = 0.06$, $\Pi_\rho = 0.95$, $\Pi_\mu = 0.01$, $\bar{d} = 0.77$, $\Lambda/R = 7.0$, $\hat{d}_0 = d_{\max}|_{\tilde{t}=0} - \bar{d} = 0.0023$; (b) $\text{La} = 66087$, $\Pi_\rho = 1.2$, $\Pi_\mu = 5.6$, $\bar{d} = 0.8$, $\Lambda/R = 7.0$, $\hat{d}_0 = 0.0025$. The Laplace number $\text{La} = \sigma R \rho_l / \mu_l^2$, $\tau_a = \mu_l R / [\sigma (1 - \bar{d})^3]$, and τ_b according to (3.1). Squares highlight time points considered in figures 7(a) and 7(b), respectively.

542 core phase. Agreement with the DNS data is good, showing that drainage of the liquid
 543 film during liquid bridge formation creates two large counter-rotating vortices, the center
 544 of which is located in the core. The ability to accurately predict these flow structures,
 545 which represent an intensification of convective transport, is relevant from the point of
 546 view of oxygen transfer in human lung capillaries as well as drying of porous media.

547 The growth of the collars in figure 3 and the associated vortices in figure 4 are driven by
 548 pressure gradients in the liquid that are imposed by variations in free-surface curvature.
 549 Figure 5 shows profiles of the axial wall pressure derivative for different time points
 550 in figures 3(b) and 3(d), i.e. for the unduloid and liquid bridge scenario, respectively.
 551 Circles in this diagram mark DNS data while the dashed (unduloid scenario) and solid
 552 (liquid bridge scenario) lines refer to model predictions. DNS data are only presented
 553 for the latest time point in each case ($\tilde{t}/\tau=5.4, 5.6$) to avoid cluttering the graph. The
 554 two earlier time points are included to illustrate the principal difference between the
 555 two evolution scenarios. In the liquid bridge scenario, the pressure derivative increases
 556 everywhere as time progresses, constantly increasing the volume of the collar by driving
 557 liquid from the film trough. By contrast, the pressure derivative for the unduloid scenario
 558 decreases with time in the region of the collar while increasing at the position of the film
 559 trough. Comparison of the two time points for this scenario shows that the pressure
 560 derivative profile increasingly flattens from within until eventually all pressure variations
 561 are nullified and the film reaches the equilibrium shape of an unduloid.

562 Turning to liquid/liquid film-fluid/core-fluid pairings, figure 6 shows time traces of the
 563 extremal core radii for a glycerol/silicone-oil (panel a) and a water/silicone-oil combi-
 564 nation (panel b). Parameter values are taken from Tai *et al.* (2011) and Piroird *et al.*
 565 (2011), respectively. We point out that the time scale in panel a is $\tau_a = \mu_l R / [\sigma (1 - \bar{d})^3]$,
 566 chosen to facilitate comparisons with Tai *et al.* (2011), while it is defined according to
 567 (3.1) in panel b. In the first case, the film fluid is significantly more viscous than the core
 568 fluid as opposed to the second case where viscosities are comparable and the viscosity
 569 level is lower. In both cases, the liquid volume is sufficiently large to cause flooding and

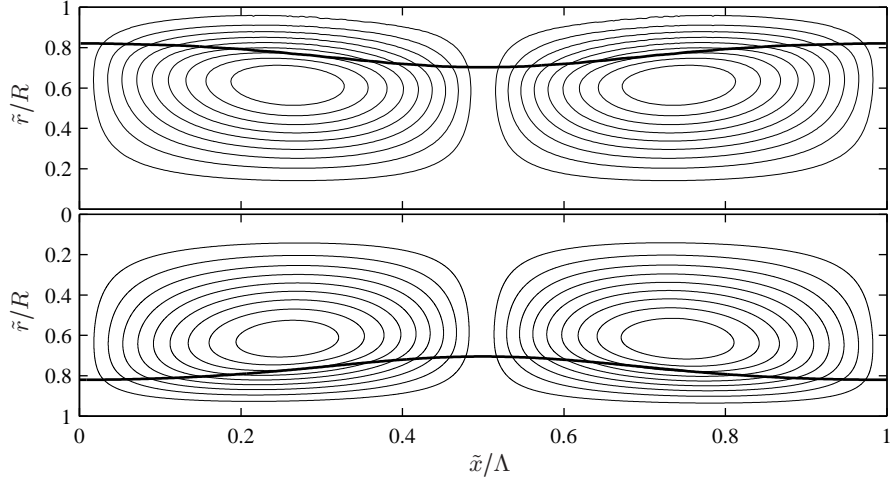
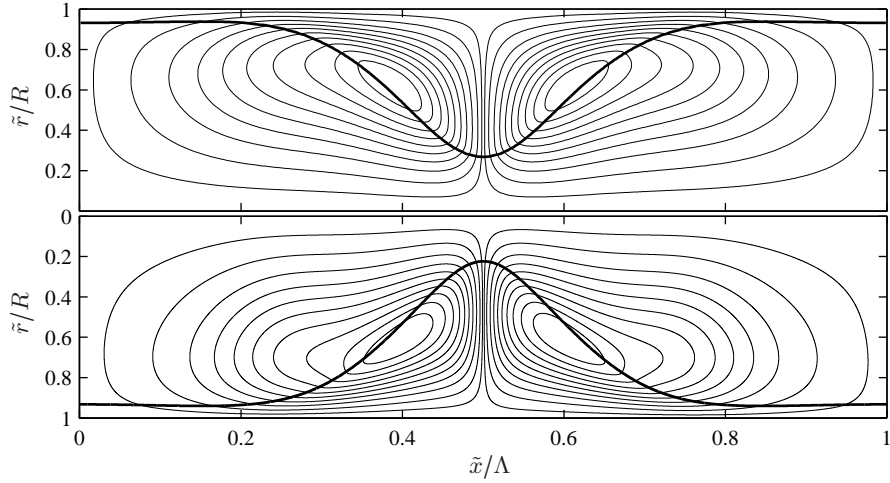
(a) Glycerol/silicone-oil: $\tilde{t}/\tau=13.8$.(b) Water/silicone-oil: $\tilde{t}/\tau=25.6$ (DNS); $\tilde{t}/\tau=25.1$ (WRIBL model).

FIGURE 7. Streamlines in the wall-fixed reference frame obtained from DNS (top) and the WRIBL model (bottom). (a) Glycerol/silicone-oil (see squares in figure 6(a) for time point); (b) Water/silicone-oil (see squares in figure 6(b) for DNS time point). Stream functions are normalized by their maximum and contour line values identical in DNS and WRIBL plots.

570 we observe more or less the same evolution as in figure 3(d). Agreement between model
 571 and DNS data is again good, the time to flooding being predicted with better accuracy
 572 here, owing to the fact that Λ/R is larger. Figure 7 depicts corresponding streamlines at
 573 selected time points and again we remark good agreement between the model and DNSs.

574 These comparisons give us confidence in the physical soundness of our WRIBL model,
 575 which we now employ for a more detailed investigation of the considered gravity-free
 576 annular-film/fluid-core arrangement.

577 3.2. Flooding dynamics: role of inertia and core fluid

578 We start by identifying the limits of simplifying assumptions that are frequently made
 579 regarding these flows, such as neglecting inertia and considering the core phase as passive.

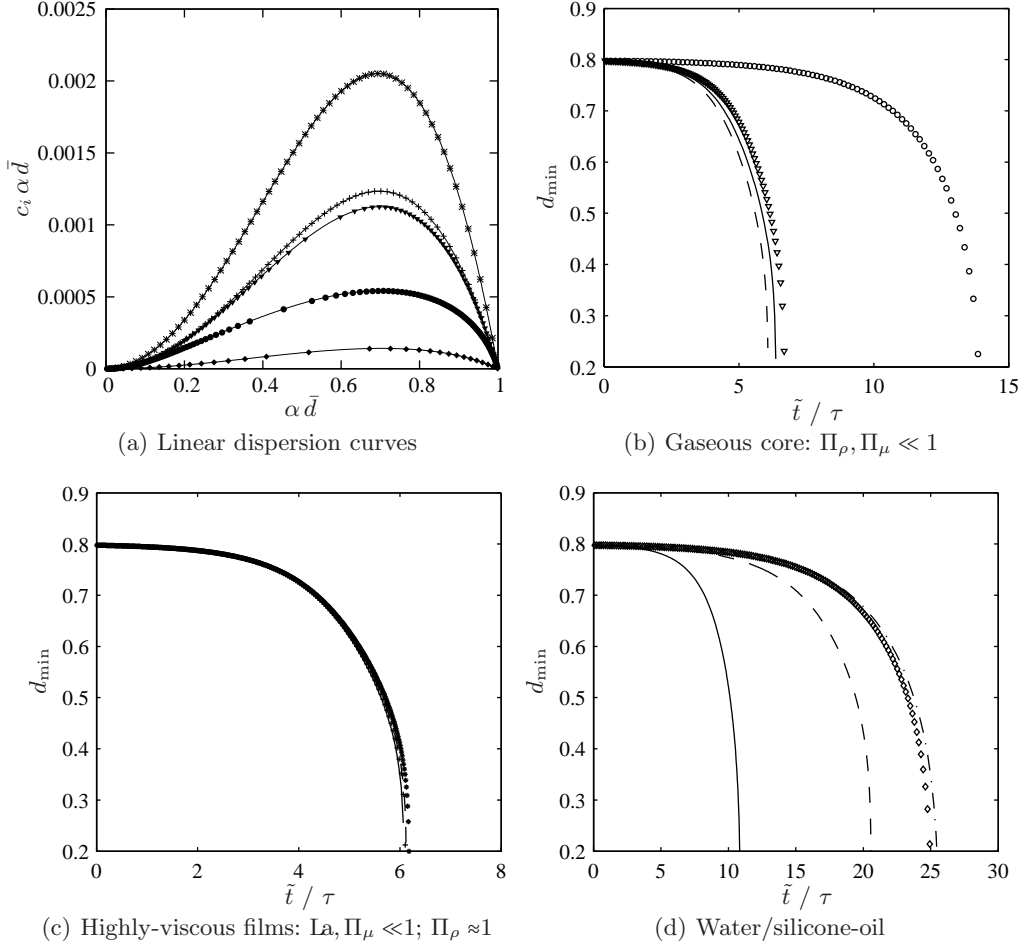


FIGURE 8. Model predictions of liquid bridge formation in different limits. (a) Linear dispersion curves obtained from the full model (symbols) and the Orr-Sommerfeld equation (lines) for different fluid pairings in table 3. \bullet : water/air; \blacktriangledown : mucus/air; $+$: oil/water; $*$: glycerol/silicone-oil; \blacklozenge : water/silicone-oil. (b) Gaseous core ($\Pi_\rho, \Pi_\mu \ll 1$). Circles (full model) and solid line (inertialess limit): water/air; triangles (full model) and dashed line (inertialess limit): mucus/air. (c) Highly-viscous films ($\text{La}, \Pi_\mu \ll 1, \Pi_\rho \approx 1$). Stars (full model) and dashed line (passive core limit): glycerol/silicone oil; pluses (full model) and solid line (passive core limit): oil/water. (d) Water/silicone-oil. Diamonds: full model; solid line: passive core; dashed line: inertialess limit; dot-dashed line: larger core fluid density.

580 Our results are summarized in figure 8, showing linear growth rates and minimal core
 581 radius time traces for a set of realistic fluid pairings: water/air and mucus/air (panel b),
 582 oil/water and glycerol/silicone-oil (panel c), and water/silicone-oil (panel d). All relevant
 583 parameters are quantified in table 3. As a basis for comparison and in contrast to table
 584 2, we have fixed $\bar{d} = 0.8$ as well as the relative wavelength $\Lambda/(\bar{d}R)$ (by setting Λ to the
 585 linearly most amplified value). Consequently, the dimensionless liquid volume $\tilde{V}_l/(\pi R^3)$
 586 is constant for all cases. In addition to calculations with realistic parameter values, panels
 587 b to d also contain results in the inertialess (vanishing fluid densities) and passive-core
 588 ($\Pi_\rho, \Pi_\mu \ll 1$) limits, respectively.

589 For the two liquid/gas pairings (panel b), the core fluid is practically passive in reality

Film/core	ρ_l (kg/m ³)	ρ_g (kg/m ³)	μ_l (Pas)	μ_g (Pas)	σ (N/m)	R (mm)	La	τ (ms)
Water/air <i>inertialess limit</i>	997.1 $\rho_l/100$	1.2 $\rho_g/100$	$8.9 \cdot 10^{-4}$	$1.8 \cdot 10^{-5}$	0.072	1.5	$1.3 \cdot 10^5$ $La/100$	10.1
Mucus/air <i>inertialess limit</i>	1098.3 $\rho_l/100$	1.2 $\rho_g/100$	$3.1 \cdot 10^{-3}$	$1.8 \cdot 10^{-5}$	0.031	1.5	5287 $La/100$	81.6
Oil/water <i>passive core limit</i>	997.1	1006 $\rho_g/1000$	0.17	$8.9 \cdot 10^{-4}$ $\mu_g/100$	0.035	0.027	0.03	71.8
Glycerol/silicone-oil <i>passive core limit</i>	1251	1191 $\rho_g/1000$	0.624	$\mu_l/100$ $\mu_g/100$	0.03	0.58	0.06	6597
Water/silicone-oil <i>passive core limit</i> <i>inertialess limit</i> <i>larger core density</i>	997.1 $\rho_l/100$	1191 $\rho_g/1000$ $\rho_g/100$ $1.5\rho_l$	$8.9 \cdot 10^{-4}$	0.005 $\mu_g/100$	0.035	1.5	66087 $La/100$	20.8

TABLE 3. Parameters for liquid bridge formation scenarios in figure 8: $\bar{d}=0.8$, $La=\sigma \rho_l R/\mu_l^2$, τ according to (3.1). The wavelength in all cases corresponds to the linearly most amplified value in figure 8(a). The values of the Reynolds number $Re_F = \rho_l R^2/(\mu_l \tau_F)$ based on the time to flooding τ_F are 17.8, 1.4 and 4.8 for the water/air, mucus/air and water/silicone-oil scenarios respectively, while $Re_F \ll 1$ for the highly viscous films.

590 so that the passive-core limit need not be investigated further. On the other hand, the
591 Laplace number, which relates inertia and driving capillary to stabilizing viscous forces, is
592 very large here and consequently, inertia is expected to be relevant. This is confirmed by
593 the core radius time traces in figure 8(b), showing inertialess predictions to underestimate
594 the time to flooding. For the water/air combination ($La \approx 10^5$) the error is significant (≈ 60
595 %), while it is smaller (≈ 10 %) for the mucus/air pairing ($La \approx 10^3$). In the inertialess
596 limit, the liquid film reacts immediately to the resulting driving force (difference between
597 capillary-induced pressure gradients and viscous stresses), which is quantified by La and
598 thus, as La increases, the inertialess prediction of the time to flooding is increasingly
599 too short. The relevance of inertia can also be inferred from the Reynolds number $Re_F =$
600 $\rho_l R^2/(\mu_l \tau_F)$ based on the time to flooding τ_F , which was obtained from figure 8. Indeed,
601 for the water/air, mucus/air and water/silicone-oil scenarios $Re_F = 17.8, 1.4$ and 4.8
602 respectively, while $Re_F \ll 1$ for the highly viscous films.

603 When the liquid film is very viscous and much more so than the core fluid, as is consid-
604 ered in figure 8(c), La is low and inertia is insignificant. In addition, viscous dissipation
605 in the core fluid is negligible compared to the film so that the core phase is effectively
606 passive. This limit is shown to give very precise predictions of the film evolution for the
607 oil/water and glycerol/silicone-oil combinations. Interestingly, all four curves in this plot
608 collapse, owing to the choice of the time scale τ (3.1), which is pertinent in the inertialess
609 passive-core limit (Johnson *et al.* 1991).

610 Figure 8(d) concerns a more complicated fluid combination, i.e. a water film and a
611 silicone oil core. In this case, La is large and the densities and viscosities of the two fluids
612 are comparable. Consequently, neither the inertialess (20 % error) nor the passive-core
613 (60% error) limit predict the film evolution accurately. As inertia clearly is relevant in this
614 case, we have also checked the influence of the density ratio by increasing the core density
615 by 50 % with respect to the liquid. The resulting time trace in figure 8(d) (dot-dashed
616 line) predicts a longer time-to-flooding than for the lower density ratio. This excludes

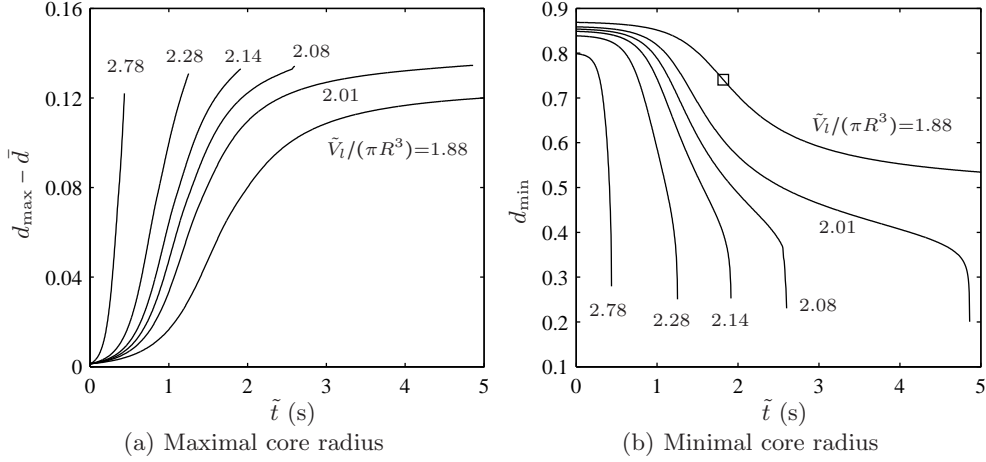


FIGURE 9. Transition between fast and slow flooding dynamics as liquid volume, controlled through $\bar{d} = [0.80, 0.84, 0.85, 0.855, 0.86, 0.87]$, decreases. All other properties are maintained constant. The film/core fluid pairing is mucus/air (Halpern & Grotberg 2003): $\text{La} = \sigma \rho_l R / \mu_l^2 = 5287$, $\Pi_\rho = 0.001$, $\Pi_\mu = 0.002$, $\Lambda/R = 7.73$, $\dot{d}_0 = d_{\max}|_{t=0} - \bar{d} = 0.0013$. The maximal liquid volume of an unduloid is $\tilde{V}_l / (\pi R^3) = 1.73$ (Everett & Haynes 1972). The square relates to figure 10.

617 any relevance of the Rayleigh-Taylor instability, which would rather increase the growth
 618 rate with increasing Π_ρ . We thus conclude that the increased physical complexity of our
 619 model, i.e. accounting for inertia, an active fluid core, and full coupling between the two
 620 phases, is indeed useful/necessary to capture the flooding dynamics of real configurations
 621 such as core-annular arrangements of water/air and water/silicone-oil.

622 3.3. Delay of flooding by viscous blocking mechanism

623 We turn now to a compelling phenomenon that we have encountered when simulating
 624 flooding scenarios for thin liquid films that are too thick to form unduloids. In these cases,
 625 $\tilde{V}_l > 1.73$ and flooding should (eventually) occur according to the criterion discussed at
 626 the beginning of this section (Everett & Haynes 1972). Figure 9 shows time traces of
 627 the perturbation amplitude $d_{\max} - \bar{d}$ and the minimal core radius d_{\min} for such a case.
 628 More precisely, parameter values correspond to one of the situations studied by Halpern &
 629 Grotberg (2003), i.e. $R = 0.3$ mm, $\text{La} = 0.01$, $\Pi_\rho = 0.001$, $\Pi_\mu = 0.002$ and $\Lambda/R = 7.73$. Different
 630 data sets in figure 9 correspond to different values of \bar{d} , which was varied to control the
 631 liquid volume (specified next to the respective graphs). At large liquid volumes ($\tilde{V}_l \geq 2.28$),
 632 the usual flooding scenario occurs. This is characterized by a progressive decline of d_{\min}
 633 until formation of a liquid bridge. When \tilde{V}_l is reduced ($\tilde{V}_l \leq 2.14$), the time traces of d_{\min}
 634 develop a point of inflexion, marking change from a progressive to a degressive growth
 635 of the liquid collar. For sufficiently large liquid volumes ($\tilde{V}_l > 2.01$), this does not prevent
 636 formation of a liquid bridge, as a second point of inflexion develops later and leads the
 637 evolution back to a progressive growth scenario. However, for $\tilde{V}_l < 2.01$ and particularly
 638 $\tilde{V}_l = 1.88$, growth at large times is entirely degressive and flooding seems to be infinitely
 639 delayed and thus effectively avoided. This is a surprising result because $\tilde{V}_l > 1.73$ and
 640 thus there are always curvature variations (and associated pressure variations) along the
 641 film surface (Everett & Haynes 1972) that drive the liquid within the film from troughs
 642 to humps (as the situation is unstable to the Plateau-Rayleigh mechanism).

643 A closer look at the evolution of the film surface is thus required and we do this for the

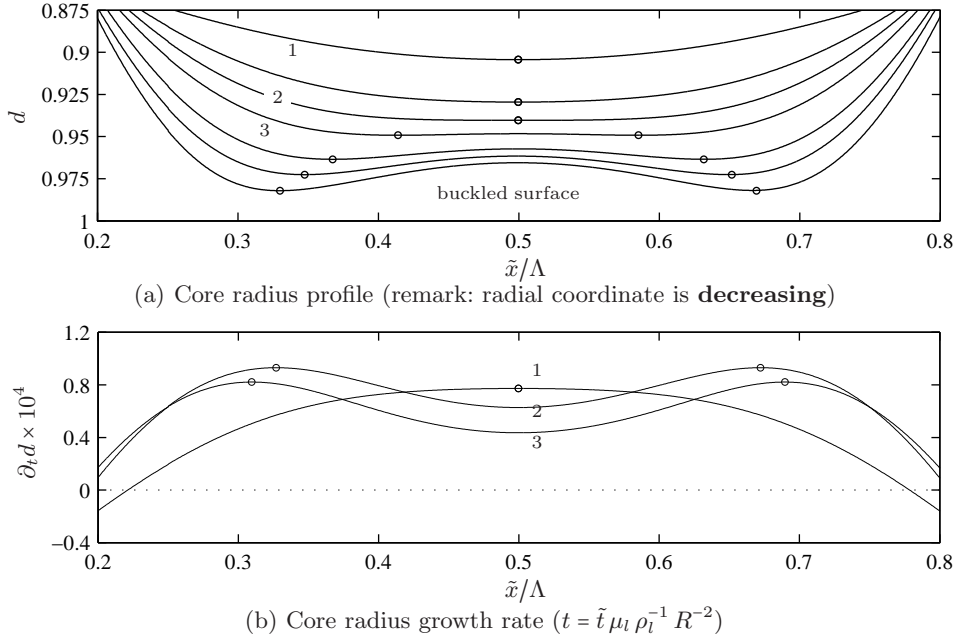


FIGURE 10. Buckling of the film trough. (a) Time evolution of the film surface for $\tilde{t}=[1.32$ (1), 1.65, 1.82 (2), 1.98 (3), 2.31, 2.64, 3.30 (bottom)] s. The uppermost four profiles show transition from an axially concave toward a convex shape, passing through a straight interface. This profile (2) signifies the onset of buckling and the corresponding time point ($t=1.82$ s) is highlighted in figure 9 with a square. (b) Profiles of the core radius time derivative at $\tilde{t}=1.32$ s (1), $\tilde{t}=1.82$ s (2) and $\tilde{t}=1.98$ s (3). Circles highlight loci of minimal core radius and maximal growth rate.

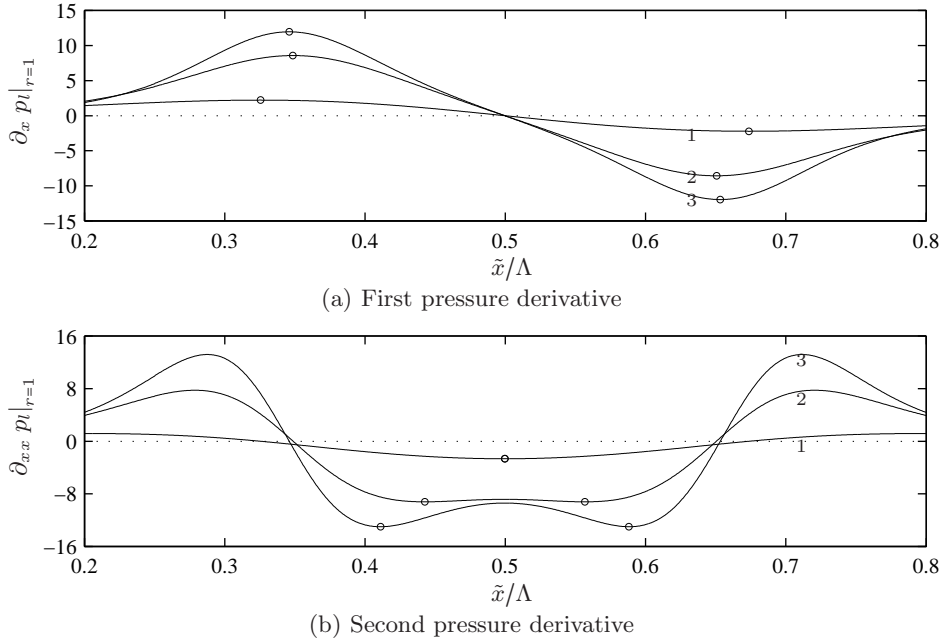


FIGURE 11. Profiles of the first (a) and second (b) axial wall pressure derivatives for the three numbered profiles in figure 10. The growth rate $\partial_t d$ in equation 3.4 is dominated by $\partial_x p_l|_{r=1}$ where $\partial_x d$ is large, while $\partial_{xx} p_l|_{r=1}$ is dominant where $\partial_x d$ is small. Circles highlight relevant extremal values.

644 case $V_l=1.88$. Due to the relevance of this case for our manuscript, we have also included a
 645 comparison with DNS data in appendix D (see figure 18). Figure 10 shows axial profiles of
 646 the film surface $d(x)$ in the vicinity of the liquid film trough, i.e. the point of maximal core
 647 radius and minimal film thickness, at different time points (remark: the radial coordinate
 648 is **decreasing** in this graph). When inspecting the different profiles from top to bottom,
 649 i.e. in the order of increasing time, a change in shape is observable. The two topmost
 650 profiles have an axially concave shape throughout, the third exhibits a flat portion in
 651 the middle and from the fourth profile onwards the film surface has buckled, creating a
 652 small lobe in the middle flanked by two new troughs that grow thinner with increasing
 653 time. The transition time point between the unbuckled/buckled shape is $\tilde{t}=1.82$ s and
 654 corresponds to the third profile from the top. This point is highlighted with a square in
 655 figure 9(b) and coincides with the inflexion point of the core radius time trace. Buckling
 656 thus causes the change in flooding dynamics and we proceed to explain its mechanism.

657 A purely kinematic view is provided in figure 10(b), depicting profiles of the core radius
 658 growth rate $\partial_t d$ at selected time points in figure 10(a). In the early stages when the liquid
 659 film is still relatively thick ($\tilde{t}=1.32$ s, profile 1), the growth rate is maximal at the trough
 660 and decreases monotonically moving outward, which tends to preserve the concave shape
 661 of the film surface. With increasing time however, flow in the film trough, the first locus
 662 to “feel” the presence of the approaching wall, is increasingly affected by viscous forces,
 663 generating a dip in growth rate there (profiles 2 and 3). In this region, the axial flow
 664 closely approaches lubrication conditions and the liquid flow rate q_l can be expressed in
 665 terms of the liquid wall pressure gradient (for convenience, we assume $\Pi_\rho=\Pi_\mu=0$ here):

$$q_l = \partial_x p_l|_{r=1} \frac{\pi Re_l}{8} [-1 + 4d^2 + d^4(-3 + 4 \log d)], \quad (3.3)$$

666 which, with the help of equation 2.2, yields the growth rate $\partial_t d$:

$$\partial_t d = Re_l [A(d) \partial_x p_l|_{r=1} \partial_x d + B(d) \partial_{xx} p_l|_{r=1}], \quad (3.4)$$

$$A(d) = \frac{1}{2} [1 + d^2(-1 + 2 \log d)], \quad B(d) = \frac{1}{16d} [-1 + 4d^2 - d^4(3 - 4 \log d)].$$

667 The monotonic functions $A(d) \geq 0$ and $B(d) \leq 0$ both approach zero as $d \rightarrow 1$. How-
 668 ever, $B(d)$ does so more rapidly than $A(d)$ and thus the growth rate $\partial_t d$ is dominated
 669 by $\partial_x p_l|_{r=1}$ for very thin films, unless the gradient $\partial_x d$ is small. Importantly however,
 670 $\partial_x d = \partial_x p_l|_{r=1} = 0$ at the film trough due to symmetry and so the second pressure deriva-
 671 tive always controls growth there. Figure 11(b) shows that $\partial_{xx} p_l|_{r=1}$ is large and negative
 672 at the film trough, explaining the initially large $\partial_t d$ there. However, as $|B(d)|$ monoton-
 673 ically decreases with increasing d (due to increasing viscous flow resistance), $\partial_t d$ at the
 674 trough must decrease with time, explaining the dip in profiles 2 and 3 of figure 10(b).

675 Viscous slowing of growth in the region of the film trough causes the flattening of
 676 the film surface discernible between profiles 1 and 2 in figure 10(a). This in turn has two
 677 consequences that are relevant for the subsequent growth dynamics: (i) At the extremities
 678 of the flat portion of profile 2 ($\tilde{x}/\Lambda \approx 0.4, 0.6$) either side of the film trough, the second
 679 pressure derivative in figure 11(b) develops minima. Because growth in the flat film
 680 region is dominated by the second pressure derivative, $\partial_t d$ there increases relative to the
 681 trough. As a consequence, the film surface buckles, forming two new troughs at these
 682 positions (profile 3 and onwards in figure 10(a)). (ii) As the flat portion of the film surface
 683 profile extends outward, the steepness $\partial_x d$ of the outlying portions ($\tilde{x}/\Lambda < 0.4, \tilde{x}/\Lambda > 0.6$)
 684 strongly increases, which, according to (3.4), amplifies growth there due to the first
 685 pressure derivative. This effect causes $\partial_t d$ in figure 10(b) to attain global maxima at

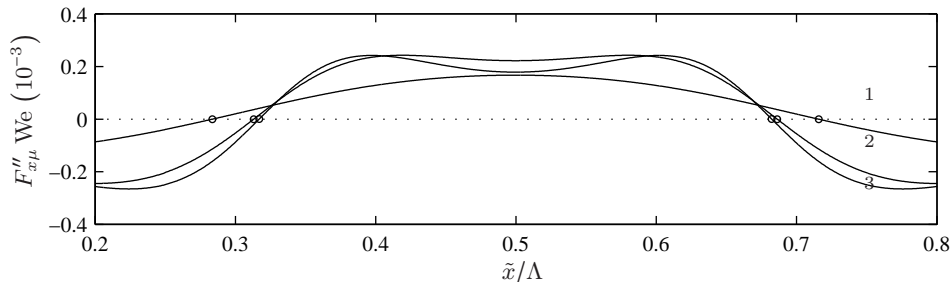


FIGURE 12. Total (dimensionless) viscous force per unit area $F''_{x\mu}$ acting on the axial cross-section of the liquid film (3.5) related to the (dimensionless) pressure jump We^{-1} across a free surface of core radius $d=1$ (the length scale being $L = R$). Negative values (circles mark changes of sign) indicate deceleration of the liquid ($\partial_x u < 0$) as it moves away from the film trough in the center (see figure 10(a) for film surface profiles). This produces an axial viscous force compressing the liquid between the considered position and its mirror on the other side of the trough.

686 $\tilde{x}/\Lambda \approx 0.3, 0.7$, where the axial pressure gradient, plotted in figure 11(b), is large and
 687 positive. This large growth rate causes the flat and later the buckled portion of the film
 688 surface to keep extending outward, explaining the gradual displacement of the buckling-
 689 induced film troughs as time progresses (profile 3 and onwards in figure 10(a)).

690 From the point of view of the flooding dynamics in figure 9(b), the most relevant
 691 feature of the buckling mechanism is that it eventually produces two very thin film
 692 troughs at $\tilde{x}/\Lambda \approx 0.3, 0.7$, which act as bottlenecks in the subsequent growth scenario.
 693 Indeed, liquid required to sustain the growth of the large collars, needs to pass through
 694 these bottlenecks, which will grow even thinner as time goes on. This explains both the
 695 extreme slowness of growth in figure 9(b) for $t > 1.82$ s (we are still considering the case
 696 $V_l = 1.88$) as well as its degressive nature.

697 In summary, unstable thin liquid films can thus drastically delay forming a liquid
 698 bridge even if their volume is too large to form an unduloid. In contrast to small-volume
 699 liquid films, which evolve into static unduloids, arrest of growth is not achieved through a
 700 decrease in the driving force (i.e. capillary pressure gradients) but rather through viscous
 701 dissipation. More precisely, the liquid film forms an interfacial shape that maximizes this
 702 dissipation by generating a buckled surface between two very thin troughs, acting as
 703 bottlenecks. This buckled surface, due to its local extrema, is not compatible with the
 704 definition of an unduloid. We thus believe that the delay of flooding observed in figure
 705 9(b) is caused by a distinct mechanism, rather than being the result of approaching the
 706 threshold for the existence of unduloids as the liquid volume decreases.

707 It is interesting to compare these observations to the drainage of small-volume liquid
 708 films investigated by Lister *et al.* (2006). Indeed, there also, thin lobes separating large
 709 collars were found to impose very slow evolution dynamics. However, in contrast to
 710 our work, Lister *et al.* (2006) considered films in the limit $V_l \rightarrow 0$, i.e. films that may
 711 form unduloids. Our observations are complementary in that they show that liquid films
 712 of sufficiently large volume that they cannot reach an equilibrium shape other than a
 713 liquid bridge can be effectively prevented from flooding by a viscous blocking mechanism.
 714 We also point out that the buckled shapes represented in figure 10(a) closely resemble
 715 the saturated interfacial shapes observed by Yiantsios & Higgins (1989) for liquid films
 716 subject to the Rayleigh-Taylor instability.

717 For completeness, we discuss the role of two other effects that immediately come to
 718 mind with regard to the buckling mechanism. Firstly, the secondary lobe emerging from

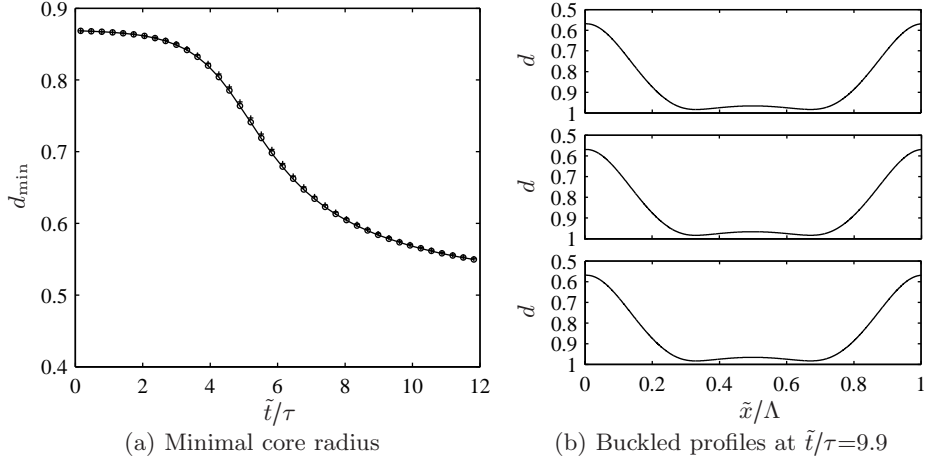


FIGURE 13. Insensitivity of the viscous-blocking mechanism to the Laplace number $\text{La} = \sigma \rho_l R / \mu_l^2$, which was varied across two orders of magnitude: $\text{La} = 91.8 = \text{La}_0$ (solid line); $\text{La} = 10 \cdot \text{La}_0$ (circles) and $\text{La} = 100 \cdot \text{La}_0$ (pluses). (a) Minimal core radius as a function of time scaled with τ according to (3.1); (b) buckled profiles at $\tilde{t}/\tau = 9.9$.

719 the buckled surface in figure 10(a) could conceivably result from a primary Plateau-
 720 Rayleigh instability of the flat film forming at the trough. However, the length of the
 721 lobe being approximately $l = 0.4 \Lambda = 3.1 R$, i.e. smaller than the circumference of the film
 722 surface there $2\pi 0.925 R = 5.8 R$, this hypothesis must be discarded. Formation of the
 723 secondary lobe, although similar in appearance, is thus mechanically different from the
 724 formation of a satellite drop in the core fluid as may occur during liquid bridge formation.
 725 In the latter case, the core radius is very small and thus the Plateau-Rayleigh mechanism
 726 dominant. Secondly, the term “buckling” in a fluid-mechanical context is generally used
 727 when viscous normal stresses cause a fluid flow confined by a free surface to deviate from
 728 its (unstable) primary configuration (Suleiman & Munson 1981; Yarin & Tchadarov 1996;
 729 Ribe 2002; Slim *et al.* 2009; Ribe 2012; Slim *et al.* 2012). In analogy to buckling of solid
 730 plates or rods, this only occurs when the viscous stresses are compressive, i.e. $2\mu \partial_x u < 0$,
 731 which means that the flow must be decelerating. To check whether the thin film in the
 732 region of the trough represented in figure 10 is indeed axially compressed by normal
 733 viscous stresses, figure 12 depicts profiles of the total (dimensionless) axial viscous force
 734 per unit area $F''_{x\mu}$ acting on the cross section of the film (more precisely, the cross section
 735 of which the normal is oriented away from the film trough):

$$F''_{x\mu} = \tilde{F}''_{x\mu} / (\rho_l U^2), \quad \tilde{F}''_{x\mu} = -\frac{1}{\pi (R^2 - \tilde{d}^2)} \int_{\tilde{d}}^R 2\pi \tilde{r} (2\mu_l \partial_{\tilde{x}} \tilde{u}) d\tilde{r}. \quad (3.5)$$

736 In figure 12, $F''_{x\mu}$ is related to a representative (dimensionless) liquid pressure P , which
 737 we have chosen as the pressure jump across a cylindrical film surface of dimensional
 738 radius R . Choosing the length and velocity scales for non-dimensionalization as $L = R$
 739 and $U = \mu_l / (\rho_l R)$, we obtain $P = \text{We}^{-1}$. Figure 12 instructs us that, although viscous
 740 compressive forces act in the outer regions either side of the film trough, their magni-
 741 tude is relatively small compared to pressure forces and thus, viscous buckling is not of
 742 significant importance here.

743 Next, we attempt to provide a quantitative criterion for the onset of the viscous-

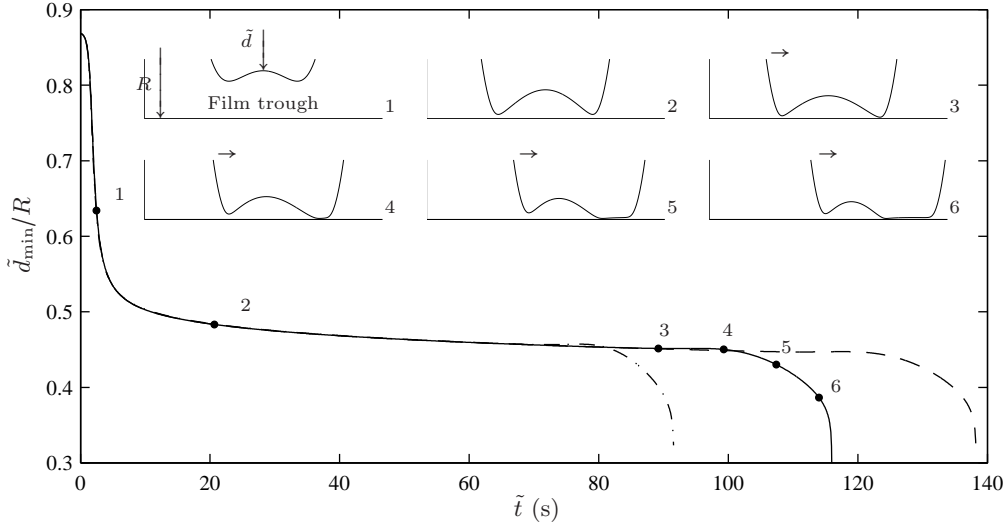


FIGURE 14. Long-time evolution of the minimal core radius for the case in figure 9(b): $\tilde{V}_i/(\pi R^3)=1.88$. Flooding occurs only at very long times due to symmetry breaking in the region of the film trough, which subsequently produces a sliding motion of the liquid film ($\tilde{t} > 70$ s). This kick-starts the growth of large liquid collars anew and eventually leads to the occlusion of the tube. These events are illustrated by inserts, showing the time evolution of the film trough in a magnified view (the horizontal line corresponds to the tube wall and the displayed axial and radial intervals are $\tilde{x}/\Lambda \in [0, 1]$ and $\tilde{r}/R \in [0.95, 1]$, respectively). The dot-dashed line relates to the limit $J_i = K_i = L_i = M_i = 0$ in (2.33), when axial normal viscous stresses are not accounted for. Different types of perturbations cause the symmetry breaking for the dashed (numerical errors) and solid/dot-dashed (minute gravitational acceleration $g_{\text{res}}=10^{-10}$ m/s²) lines, respectively.

744 blocking mechanism. If it is assumed that the wavelength of the free-surface perturbation
 745 corresponds to the linearly most amplified value, i.e. $\Lambda/R \approx 2\pi \bar{d}^{1/2}$, and that the core-
 746 phase is more or less passive, i.e. $\Pi_\rho, \Pi_\mu \ll 1$, there are only two remaining influencing
 747 parameters: the mean core radius \bar{d} and the Laplace number $\text{La} = \sigma \rho_l R / \mu_l^2$. While the
 748 effect of \bar{d} has been previously established in figure 9, figure 13 illustrates the effect of
 749 La . Intriguingly, the viscous-blocking mechanism seems to be insensitive to La , which
 750 after all was varied over two orders of magnitude. Although the dimensional temporal
 751 growth quickens with increasing Laplace number, the dimensionless core-radius-time-
 752 traces in panel (a) perfectly collapse if the time scale τ according to (3.1) is used for
 753 non-dimensionalization. Consequently, all time traces illustrate the same physics, i.e. a
 754 point of inflexion and a degressive growth behaviour at large times, indicating viscous-
 755 blocking. Moreover, panel (b) shows that the same buckled interfacial shape is attained
 756 for all La values at sufficiently large times. We thus conclude that the limit $\bar{d} \gtrsim 0.86$
 757 established in figure 9(b) is a sufficient criterion for the onset of viscous blocking.

758 Although the viscous blocking mechanism discussed above drastically slows down the
 759 growth of large liquid collars, the thermodynamic criterion of Everett & Haynes (1972)
 760 predicts that eventually, i.e. for sufficiently long times, the liquid film in figure 9(b)
 761 ($V_i=1.88$) must form a liquid bridge. To investigate the dynamics leading to this event, we
 762 have performed several long-time model simulations. Figure 14 depicts time traces of the
 763 minimal core radius obtained from these long-time simulations. We start by concentrating
 764 on the solid line, which shows that, for times exceeding the interval displayed in figure
 765 9(b), d_{min} continues to grow degressively for a very long duration, until reaching a plateau

766 value at $\tilde{t} = 90$ s. During this time, the film thickness profile remains almost unchanged.
 767 Subsequently, starting at $\tilde{t} = 90$ s, the dynamics in the region of the film trough start to
 768 play a decisive role. This is illustrated by numbered inserts in figure 14, displaying the
 769 time evolution of the film surface in this region at representative time points in the core
 770 radius time-trace (highlighted by filled circles and numbers corresponding to respective
 771 inserts). It shows that, from the third profile onwards, the symmetry of the film surface is
 772 broken, producing a shallower trough on the right than on the left. At the same time, the
 773 film surface starts to slide to the right. This motion further increases the non-symmetry,
 774 whereby the right trough evolves into a very thin and increasingly elongated residual film,
 775 while the left trough noticeably thickens. Thereby, the elongated residual film drains into
 776 the neighbouring large liquid collar as a result of its small axial interfacial curvature.
 777 This causes the latter to grow and eventually form a liquid bridge.

778 **In order for symmetry to break in a macroscopically symmetrical system as our static**
 779 **film/core arrangement, two conditions must be fulfilled: (i) the film shape shown in insert**
 780 **2 of figure 14 must be unstable to small non-symmetrical perturbations, and (ii) such per-**
 781 **turbations must exist in the first place.** In any numerical simulation, the accumulation of
 782 numerical errors over long simulation times eventually produces sufficiently large pertur-
 783 bations to disturb an unstable flow. In our case, this is demonstrated by the dashed line
 784 in figure 14, where symmetry-breaking occurs solely due to numerical errors. However,
 785 the nature and amplitude of numerical errors are difficult to control in a numerical simu-
 786 lation as they depend on many factors, ranging from minute changes in resolution to the
 787 type of machine the simulation is run on. In our specific case, this can change the sliding
 788 direction of the liquid film once the symmetry has been broken. To exert more control
 789 on the source of perturbations eventually causing the symmetry breaking, the simulation
 790 underlying the solid line in figure 14 (as well as the dot-dashed line) was performed with a
 791 minute residual gravitational acceleration $g = g_{\text{res}} = 10^{-10}$ m/s² by accordingly setting the
 792 Froude number $\text{Fr} = U/(gR)^{1/2}$ in equation (2.33) (this also applies to the simulations
 793 in figures 15 to 17). Compared to the purely gravity-free simulation (dashed line) the
 794 temporal evolution is identical in the early stages and differs only in terms of the even-
 795 tual onset of symmetry breaking as well as the direction of the resulting sliding motion
 796 of the liquid film. Indeed, in the simulation with residual gravity (solid line), the film
 797 always slides in the direction of g_{res} (which we have checked by testing $g = -g_{\text{res}}$) and
 798 the onset of symmetry breaking occurs somewhat earlier than in the purely gravity-free
 799 case, where it is exclusively caused by numerical errors. Interestingly, residual gravity
 800 may actually be present in space experiments (Hamacher *et al.* 1987) due to “g-jitter”
 801 (typically acceleration variations of $10^{-4}g_{\text{earth}}$), and we see here that it may be strong
 802 enough to break the symmetry of a static film/core arrangement. Our simulations with
 803 and without residual gravity also lead us to conclude that symmetry breaking results
 804 from an unstable film surface configuration, when the newly formed troughs in figure 14
 805 (see inserts) become very thin. **In our numerical code, a centred second-order finite dif-**
 806 **ference scheme was used for spatial and an adaptive time step Crank-Nicholson scheme**
 807 **for time discretization. As opposed to Lister *et al.* (2006), no local spatial refinement of**
 808 **very thin film regions was performed, our axial grid being equidistant. As a consequence,**
 809 **our simulations required a large number of grid points to resolve the thin-film-dynamics.**
 810 The wavelength of the film in figure 14 was axially resolved with $N_x = 500$ points and grid
 811 dependence checked, for the solid line, by comparing with a $N_x = 2000$ simulation. The
 812 onset of sliding is only slightly affected (i.e. slightly delayed) by this fourfold refinement.

813 Interestingly, axial normal viscous stresses play an important role in the dynamics of
 814 the film trough evolution. This is illustrated by the dot-dashed line in figure 14, which
 815 represents data obtained with our model in the limit $J_i = K_i = L_i = M_i = 0$ of (2.33), i.e.

816 when axial normal viscous stresses are not accounted for. Indeed, this first-order model
 817 predicts flooding at a much earlier time than the full formulation, an observation in
 818 line with studies of falling liquid films where first-order integral boundary layer models
 819 have been shown to over-predict the amplitude of capillary waves preceding large wave
 820 humps (Ruyer-Quil & Manneville 2000). In our case, we have checked that the inclusion
 821 of viscous stresses mainly affects the onset of the symmetry breaking in the film trough
 822 region. We thus conclude that the (simplified) second-order WRIBL model we have in-
 823 troduced in this manuscript is necessary to accurately predict the nonlinear dynamics of
 824 gravity-free liquid-film/core-fluid arrangements in narrow tubes.

825 Finally, it is to be expected that the symmetry breaking dynamics in the film trough
 826 generate intricate flow structures in the core phase. These can be captured by our model,
 827 which fully accounts for both phases. We proceed to a detailed investigation of the core
 828 flow dynamics as well as their interaction with the liquid film in the following section.

829 3.4. Low-frequency core flow oscillations

830 To conclude this section, we consider the dynamics of the core flow and its interaction
 831 with the liquid film. For this, we prescribe a harmonic temporal oscillation of the total
 832 flow rate in our model simulations:

$$q_{\text{tot}} = q_l + q_g = 2\pi f L_T (\pi R^3) \sin(2\pi f t). \quad (3.6)$$

833 For the case of gravity-free liquid films in interaction with a gaseous core this condition
 834 amounts to imposing the core flow rate q_g , because $\Pi_\mu \ll 1$ and thus $q_g \gg q_l$. The
 835 control parameters in (3.6) are $L_T = \tilde{L}_T/R$, denoting the dimensionless stroke length (i.e.
 836 the stroke required to generate the oscillating flow with a piston pump), as well as
 837 the dimensionless oscillation frequency f . We recall that Halpern & Grotberg (2003)
 838 considered a similar situation in their investigation of pulmonary liquid films. However,
 839 the model they employed was limited to high oscillation frequencies f , which the authors
 840 found to produce a stabilizing effect regarding the formation of liquid bridges. We on the
 841 other hand consider low oscillation frequencies, of the order imposed by the breathing
 842 rate in human lungs ($\tilde{f} \approx 1/3$ Hz). In this range, we find the core flow oscillation to have
 843 a *destabilizing* effect and thus our work is complementary to Halpern & Grotberg (2003).

844 We start by setting $L_T = 0$, whereby we recover the flow scenario represented in figure
 845 14, and investigate the flow patterns produced in the core flow during the symmetry-
 846 breaking and sliding episodes discussed in the previous subsection. Accordingly, figure
 847 15 represents streamlines for four representative time points in figure 14, i.e. $t=1.98$ s,
 848 66.09 s, 84.27 s and 99.14 s. In figure 15(a), showing the earliest time, the flow pattern
 849 remains symmetrical. It is characterized by two counter-rotating vortices driven by the
 850 growth of the liquid collar, which is fed by the film troughs on either side. As these film
 851 troughs grow thinner (panel b), the two vortices develop a radially elongated core. At the
 852 same time, symmetry in the flow pattern is lost, whilst one of the two vortices expands
 853 sideways, compressing its neighbour in the process. Interestingly, the film surface still
 854 appears symmetrical at this stage, at least to the eye (see also figure 14). Then, as the
 855 left film trough in figure 15(c) (the right film trough in profile 4 of figure 14) becomes
 856 significantly more pronounced than its counterpart, the left vortex starts to pinch-off.
 857 This eventually produces a cellular pattern of four vortices, as shown in figure 15(d).
 858 As time progresses (not shown here), the left film trough increasingly flattens (see right
 859 trough in profile 6 of figure 14), producing an increasing number of counter-rotating
 860 vortices at that position.

861 Turning to a more complicated scenario, figure 16 compares the case of an oscillating
 862 core flow, $\tilde{f} = 1/3$ Hz and $\tilde{L}_T = 7.73R$, with the quiescent core case in figure 14. **Panel**

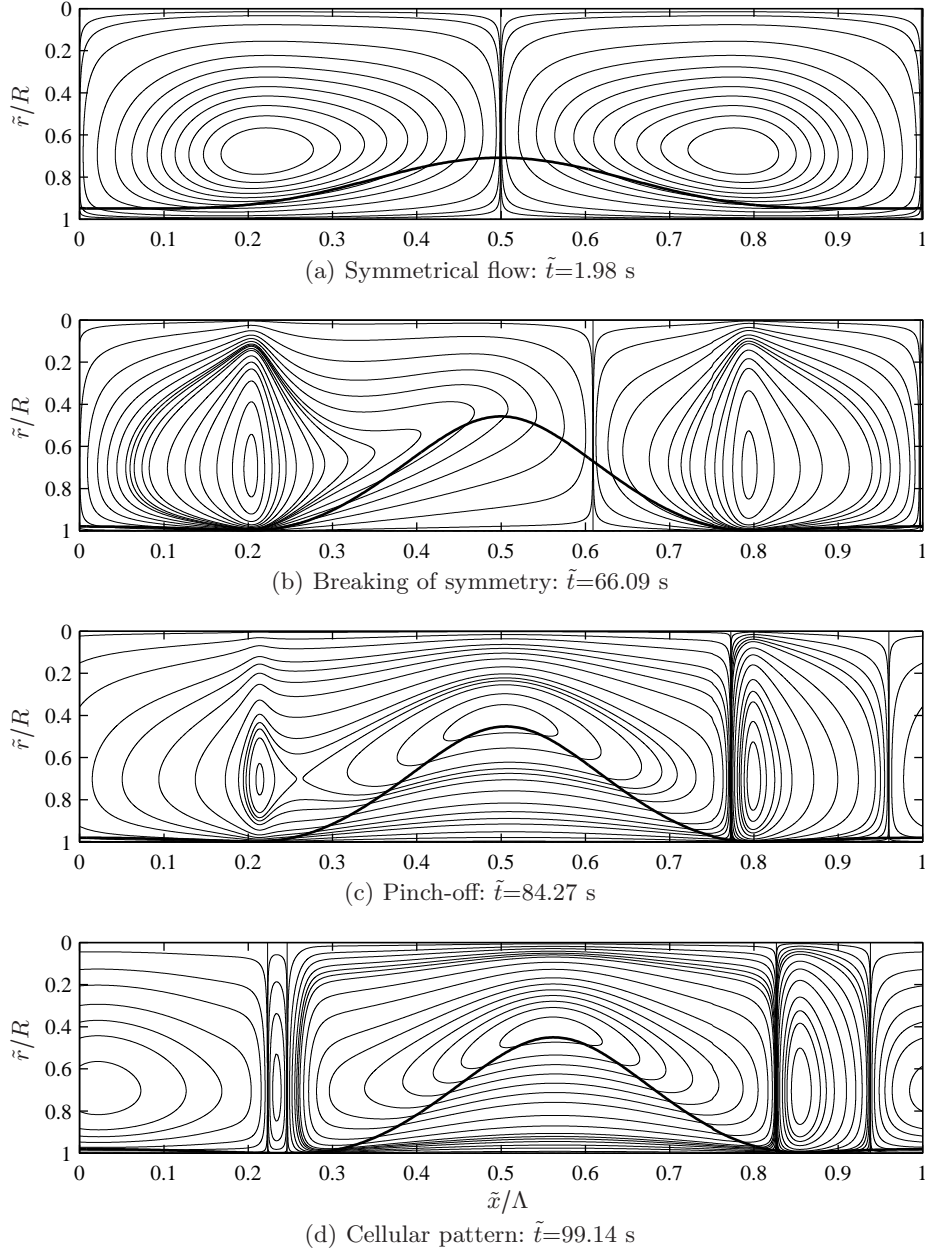


FIGURE 15. Effect of the symmetry-breaking and sliding episodes in figure 14 on the flow pattern in the liquid film and core flow. Streamlines are shown at time points $\tilde{t}=1.98$ s, 66.09 s, 84.27 s, and 99.14 s. Liquid film conditions correspond to figure 14, while for the core flow (3.6) $L_T = 0$.

863 16(a) represents time traces of the minimal core radius, showing that the onset of flooding
 864 occurs drastically sooner in the presence of an oscillatory core flow. We also note that the
 865 dot-dashed lines, which were obtained from the first-order model ($J_i = K_i = L_i = M_i = 0$
 866 in equation 2.33), confirm the importance of accounting for streamwise normal viscous

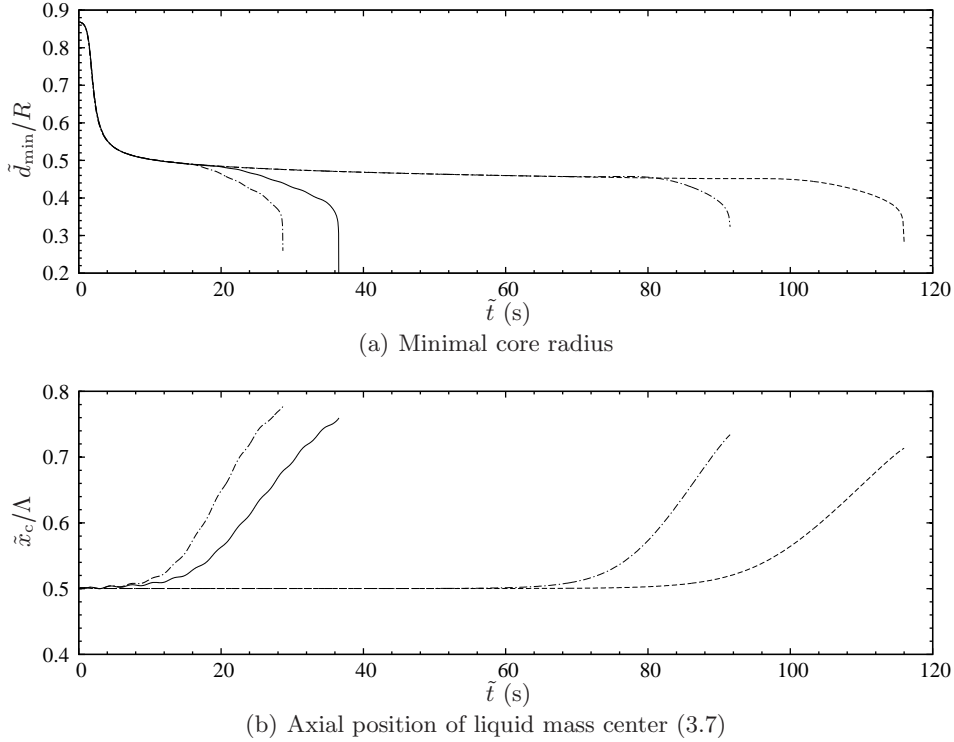


FIGURE 16. Effect of an oscillating core flow (3.6) on liquid film dynamics. Time traces of the minimal core radius (panel a) and the axial position of the center of liquid mass (panel b) according to (3.7). Dashed line: no core flow oscillation ($\tilde{L}_T=0$); solid line: core flow oscillation with $\tilde{f}=1/3$ Hz, $\tilde{L}_T=7.73 R$; dot-dashed lines: corresponding first-order model predictions ($J_i = K_i = L_i = M_i = 0$ in equation 2.33).

867 stresses, as both lines significantly deviate from the respective full-model results. The
 868 earlier onset of flooding in the case with core flow oscillations results from an earlier
 869 onset of the axial sliding observed in figure 14. This is shown in panel 16(b), displaying
 870 time traces of the axial position x_c of the liquid center of mass for the two cases in
 871 subfigure 16(a):

$$x_c = \frac{\int_d^{\Lambda/R} \pi (1 - d^2) x dx}{\int_d^{\Lambda/R} \pi (1 - d^2) dx}. \quad (3.7)$$

872 This plot confirms that sliding occurs earlier for the case with core flow oscillation.
 873 Moreover, the signature of this oscillation is discernible in the corresponding time trace
 874 of x_c . This shows that the core flow causes the film to briefly move back and forth in the
 875 very early stages before the sliding motion sets in, whereafter the core flow merely causes
 876 a periodic slowing and accelerating of this motion. **The earlier onset of sliding results
 877 from an earlier break-down of symmetry due to the back and forth motion imposed by
 878 the core flow. This oscillatory state is more unstable with respect to the minute residual
 879 gravity present in our simulations (which once again determines the direction of the
 880 sliding motion) due to the effect of axial inertia.** Meanwhile, the dot-dashed lines in
 881 subfigure 16(b) once again confirm the importance of axial normal viscous stresses.

882 Finally, we use our full two-phase model to investigate the time evolution of the flow

883 pattern in the presence of core flow oscillations. Figure 17 represents streamlines at four
 884 representative time points for the case with core flow oscillation in figure 16, i.e. $\tilde{f}=1/3$
 885 Hz and $\tilde{L}_T=7.73 R$ in (3.6). These time points are highlighted with squares in the first
 886 panel of the figure, displaying time traces of the total (solid line) and core (filled circles)
 887 flow rates. Incidentally, this plot confirms the above-introduced conjecture that the total
 888 flow rate oscillation (3.6) amounts to imposing an oscillation of the core flow rate, as
 889 indeed the two time traces are indistinguishably close.

890 The first two streamline plots in figure 17 correspond to the early stages of the liquid
 891 film evolution (see also figure 16(a)). In this stage, the growth rate of the liquid collar is
 892 large and the liquid flow dominated by the growth dynamics, i.e. the draining of the film
 893 trough towards the liquid collar. This produces a cellular flow similar to that in figure
 894 15(a), at least within the liquid. However, the flow pattern in the core is quite different
 895 and strongly affected by the temporal oscillation. Indeed, small vortices intermittently
 896 form on either side of the liquid collar depending on the direction of the core flow. More
 897 precisely, the vortices occur on the downstream side of the collar. Once, the growth of
 898 the liquid collar has slowed, the core flow influences the liquid flow pattern to a larger
 899 extent, as shown in the last two streamline plots in figure 17. In the fourth panel, the core
 900 flow is directed from right to left. The liquid film however is moving to the right as the
 901 sliding motion discussed with respect to figure 16(b) has already begun. These opposing
 902 flow directions produce a vortex in the crest of the liquid collar, circulating liquid within
 903 the film in counter-clockwise direction. At this stage, the film trough on the left of the
 904 collar has already become very thin, generating a small counter-clockwise vortex at this
 905 position (see insert, showing magnified view). In the last panel of figure 17, the core flow
 906 is oriented from left to right and thus supports the liquid sliding motion. Interestingly,
 907 liquid in the elongated film trough (which has significantly elongated at this stage) flows
 908 from right to left, creating a separation zone, which is further subdivided into several
 909 clockwise vortices.

910 4. Conclusion

911 We have considered the axisymmetric arrangement of a liquid film, lining the inner
 912 surface of a narrow cylindrical tube, in interaction with an active core fluid flow. For
 913 this configuration, we have derived a (simplified) second-order low-dimensional model
 914 by applying the long-wave weighted residual integral boundary layer (WRIBL) approach
 915 (Ruyer-Quil & Manneville 2002; Kalliadasis *et al.* 2012) to both fluid phases, while fully
 916 accounting for inter-phase coupling. In this, the current work is an extension of the
 917 work by Dietze & Ruyer-Quil (2013), who considered planar two-phase channel flows.
 918 The model accounts for inertia as well as axial viscous diffusion, considers full inter-
 919 phase coupling, and allows to reconstruct the flow field in both phases. It consists of
 920 three evolution equations (2.33) and (2.2) that relate the film and core flow rates to
 921 the interface position. These are completed by an adjoined pressure equation (2.34) that
 922 can be used for an a posteriori evaluation of the pressure distribution or to impose
 923 an integral condition on the pressure drop. Special care has been taken to formulate
 924 mathematical expressions involved in the model equations succinctly (see appendices A
 925 to C). We have derived our model for the most general case in figure 1 but apply it in this
 926 manuscript only to the static film/core arrangement displayed in figure 1(a). Thereby, we
 927 have concentrated on the phenomenon of flooding, when the Plateau-Rayleigh instability
 928 causes the liquid film to drain into collars that may become sufficiently large to generate a
 929 liquid bridge occluding the tube cross-section. Extensive comparison with linear stability
 930 calculations and non-linear two-phase DNSs, shows satisfying agreement.

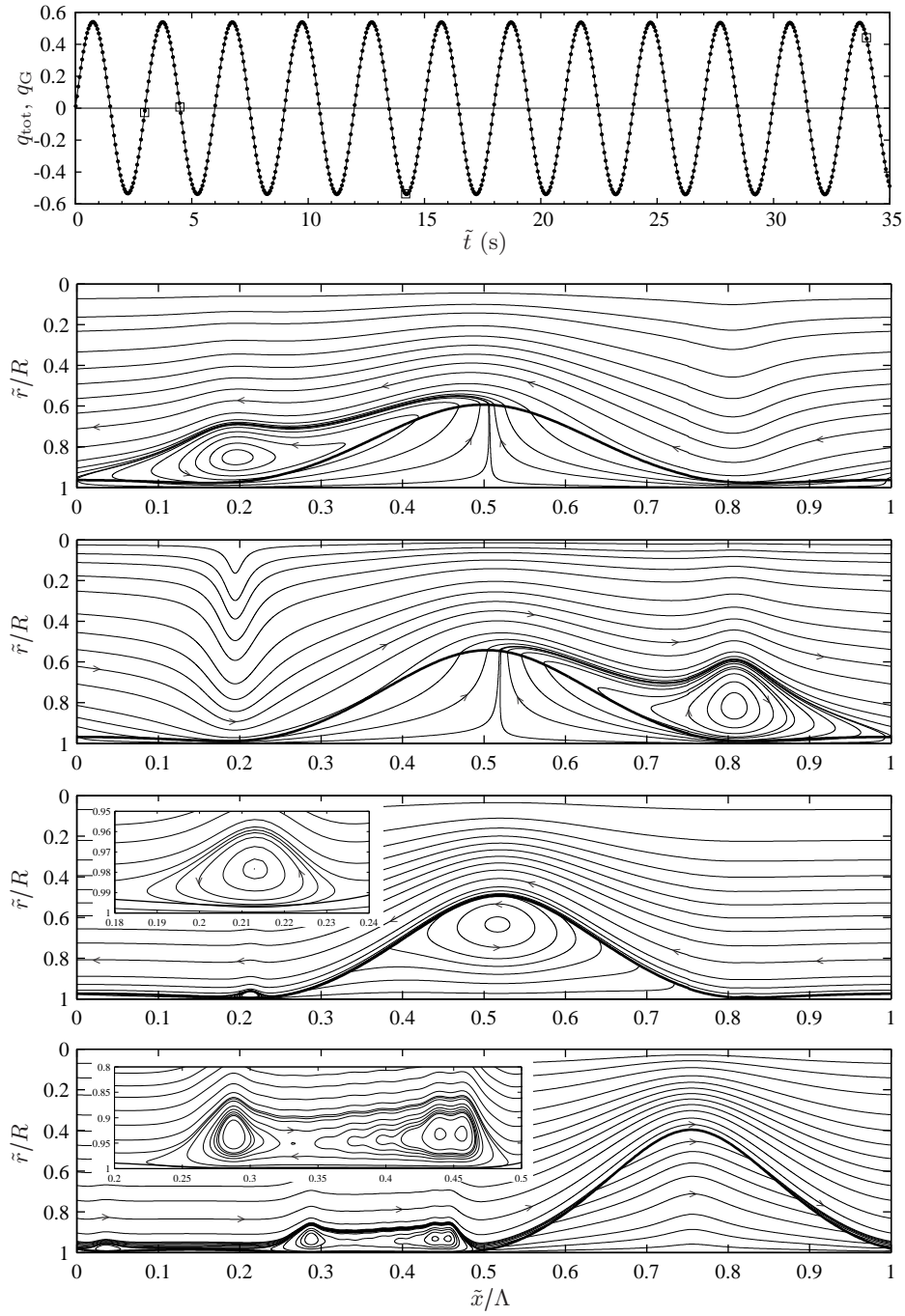


FIGURE 17. Flow patterns for the case of an oscillating core flow (3.6) in figure 16 at time points $\tilde{t}=2.97$ s, 4.49 s, 20.00 s, and 34.04 s (as displayed from top to bottom). Inserts show a magnified view of the film trough region. The first subfigure shows the time evolution of the total (solid line) and core (filled circles) flow rate, highlighting the time points of the streamline plots with squares. Flow rates are non-dimensionalized with $\mu_l R/\rho_l$.

931 Although gravity-free liquid films in narrow tubes have received considerable attention,
 932 the new contributions of our model have enabled us to elucidate a number of novel/salient
 933 physical features: *(i)* We have found that accounting for inertia as well as full inter-phase
 934 coupling is essential to accurately predict the temporal evolution of flooding for fluid
 935 combinations that are not dominated by viscosity. Examples of such combinations are
 936 water/air and water/silicone-oil; *(ii)* We have identified a viscous blocking mechanism
 937 that drastically delays the onset of flooding in thin films which are too thick to form un-
 938 dulooids (i.e. undulated equilibrium shapes). This mechanism results from a buckling of
 939 the residual film between two liquid collars, generating two very thin film troughs where
 940 dissipation is increased and growth practically arrested. Only at very long times does
 941 flooding eventually occur (as predicted by thermodynamic arguments), when symmetry
 942 breaking in the film trough region causes a sliding motion which kick-starts growth of
 943 the liquid collars anew. We have found that streamwise viscous diffusion is essential to
 944 accurately capture this mechanism. During the sliding motion, the residual film on the
 945 trailing-side of the liquid collar increasingly thins out and elongates, producing an in-
 946 creasing number of vortices in the core flow by ongoing subdivision. We point out that
 947 the observed sliding motion is similar to that observed by Lister *et al.* (2006) in very
 948 thin non-flooding liquid films; *(iii)* In the presence of a low-frequency oscillating core
 949 flow, as may occur in human pulmonary airways, the sliding-induced flooding mecha-
 950 nism is initiated at a much earlier stage. In this case, vorticity-carrying structures occur
 951 intermittently on either side of the liquid collars, in-phase with the core flow oscillation.

952 Compared to previous modelling works, our model displays a number of novel/salient
 953 features. *(a)* By accounting for inertia, the model allows to capture film flow scenarios
 954 that do not satisfy the creeping flow assumption. This is particularly relevant for flooding
 955 situations in gravity-free films and, incidentally, is a basic requirement to capture surface
 956 waves in falling liquid films; *(b)* The model treats both phases equally and fully accounts
 957 for inter-phase coupling, without imposing any restrictions on the fluid combination. As
 958 opposed to passive-core models, it can thus treat fluid combinations where the film vis-
 959 cosity is not dominant, e.g. water/silicone-oil. Moreover, consistent account of inter-phase
 960 coupling conditions enables a proper reconstruction of the velocity field in both phases.
 961 This is relevant e.g. for the investigation of heat/mass transfer intensification by interfacial
 962 deformations; *(c)* Our model includes an adjoined equation for the axial derivative
 963 of the interfacial core-fluid pressure, enabling to predict the pressure drop in the case
 964 of imposed flow rate or to impose a driving pressure difference. This allows to consider
 965 gravity- and/or pressure-driven flows in the respective phases, e.g. gravity-driven films in
 966 interaction with a counter-current core flow; *(d)* Our model does not assume thin films
 967 in relation to the tube radius and can thus predict large-amplitude interfacial deforma-
 968 tions up to the point of flooding; *(e)* By accounting for axial viscous diffusion, our model
 969 can accurately predict the dynamics of the film trough when this grows extremely thin,
 970 which is relevant e.g. for the sliding-induced flooding mechanism in gravity-free films; *(f)*
 971 Finally, our model allows calculations at drastically reduced computational cost in com-
 972 parison to full DNSs and thus represents a valuable tool for the elucidation of underlying
 973 physical mechanisms as well as the design of applications involving liquid-film/fluid-core
 974 configurations in narrow tubes. The above-mentioned sliding-induced flooding mecha-
 975 nism is a good case in point, as it is associated with locally extremely thin liquid films
 976 and very long evolution times. DNS of such a scenario is truly prohibitive.

977 In future work, we plan to use our two-phase model to study flooding of narrow tubes
 978 by falling liquid films (Trifonov 1992; Dao & Balakotaiah 2000) under the influence
 979 of a co-/counter-current gas flow. The model can also be applied to study nonlinear
 980 regimes in pressure-driven core-annular flow (Aul & Olbricht 1990) and may be expanded

981 to consider the formation of Taylor bubbles (Piroird *et al.* 2011) by incorporating a
982 disjoining pressure term (Thiele *et al.* 2013; Mayo *et al.* 2013) in (2.33).

983 **Acknowledgements**

984 G.F.D. acknowledges financial support from DAAD (Deutscher Akademischer Aus-
985 tauschdienst) and the CNRS institute INSIS (Institut des sciences de l'ingénierie et des
986 systèmes). C.R.Q. acknowledges financial support from Institut Universitaire de France.

987 **Appendix A: Coefficients of integral momentum equation**

988 Introducing the conventions $\Pi_{\rho,l} = 1$, $\Pi_{\rho,g} = \Pi_{\rho}$, $\Pi_{\mu,l} = 1$, $\Pi_{\mu,g} = \Pi_{\mu}$, $\varepsilon_l = 1$, $\varepsilon_g = -1$
 989 and $f_{kd} = f_{kk}|_{r=d}$, as well as the integrals ϕ_{ijk} , Φ_{ijkm} and Υ_{ijkm} , which are defined in
 990 appendix C, the coefficients of the model equation (2.33) are:

$$S_i = \Pi_{\rho,k} \varepsilon_m \phi_{imk}, \quad (4.1)$$

$$F_{ij} = \Pi_{\rho,k} \varepsilon_m (\Upsilon_{mijk} - \Phi_{mijk}) + \frac{1}{2\pi d} \Pi_{\rho,i} \varepsilon_j \varepsilon_k a_{ijm} \phi_{mkj}, \quad (4.2)$$

$$G_{ij} = \frac{\Pi_{\rho,m} \varepsilon_p}{2} \{a_{imk} (\Upsilon_{pjkm} - \Phi_{pjkm}) + a_{jmk} (\Upsilon_{pikm} - \Phi_{pikm})\}, \quad (4.3)$$

$$J_i = \Pi_{\mu,j} \left\{ 2C_{ij} \varepsilon_j - \frac{2}{\pi d^3} a_{ijj} + \frac{1}{\pi d^2} b_{ijj} + \frac{a_{ijk} \varepsilon_j}{d} [-4f_{kd} + 2(1 - \delta_{jm}) f_{md} + 2d \partial_r f_{kj d}] \right. \\ \left. + a_{ijk} \varepsilon_j \partial_r f_{kj d} + b_{ijk} [2\varepsilon_m \phi_{mkj} + \varepsilon_j \varepsilon_k^2 (2f_{kd} + (\delta_{jm} - 1) f_{md})] \right. \\ \left. - 8\pi d a_{ijk} \varepsilon_j f_{kd} \varepsilon_m f_{md} \right\}, \quad (4.4)$$

$$L_i = \Pi_{\mu,j} \left\{ \frac{1}{\pi d^2} a_{ijj} + a_{ijk} [2\varepsilon_m \phi_{mkj} + \varepsilon_j (2f_{kd} + (\delta_{jm} - 1) f_{md})] \right\}, \quad (4.5)$$

$$K_i = 2L_i - \frac{2\Pi_{\mu,i}}{\pi d^3} - \frac{2}{d} \varepsilon_i [2\Pi_{\mu,i} f_{id} + \Pi_{\mu,j} (\delta_{jm} - 1) f_{md}] \\ + 8d\pi (\Pi_{\mu} - 1) f_{id} \varepsilon_j f_{jd}, \quad (4.6)$$

$$M_i = \frac{\Pi_{\mu,i}}{\pi d^2} + 2\varepsilon_j \Pi_{\mu,k} \phi_{ijk} + \varepsilon_i [2\Pi_{\mu,i} f_{id} + \Pi_{\mu,j} (\delta_{jm} - 1) f_{md}]. \quad (4.7)$$

991 **Appendix B: Coefficients of pressure equation**

992 Applying the same conventions as in appendix A, the coefficients of equation 2.34 are:

$$S_i = \Pi_{\rho,k} \varepsilon_m^2 \phi_{imk}, \quad (4.1)$$

$$F_{ij} = \Pi_{\rho,k} \varepsilon_m^2 (\Upsilon_{mijk} - \Phi_{mijk}) + \frac{1}{2\pi d} \Pi_{\rho,i} \varepsilon_j \varepsilon_k^2 a_{ijm} \phi_{mkj}, \quad (4.2)$$

$$G_{ij} = \frac{\Pi_{\rho,m} \varepsilon_p^2}{2} \{a_{imk} (\Upsilon_{pjkm} - \Phi_{pjkm}) + a_{jmk} (\Upsilon_{pikm} - \Phi_{pikm})\}, \quad (4.3)$$

$$J_i = \Pi_{\mu,j} \left\{ 2C_{ij} \varepsilon_j - \frac{2}{\pi d^3} a_{ijj} + \frac{1}{\pi d^2} b_{ijj} - 2 \frac{a_{ijk} \varepsilon_j}{d} [f_{md} \delta_{kj} \varepsilon_m^2 + f_{kd} \varepsilon_j] \right. \\ \left. + b_{ijk} [2\varepsilon_m^2 \phi_{mkj} - \varepsilon_j (-2f_{kd} + \varepsilon_k (\delta_{jm} - 1) f_{md})] \right. \\ \left. - 8\pi d a_{ijk} \varepsilon_j f_{kd} \varepsilon_m^2 f_{md} \right\} + \Pi_{\mu,k} a_{ijk} \partial_r f_{kd} (4\varepsilon_j - 1), \quad (4.4)$$

$$L_i = \Pi_{\mu,j} \left\{ \frac{1}{\pi d^2} a_{ijj} + a_{ijk} [2\varepsilon_m^2 \phi_{mkj} - \varepsilon_j (-2f_{kd} + \varepsilon_k (\delta_{jm} - 1) f_{md})] \right\}, \quad (4.5)$$

$$K_i = 2L_i - \frac{2\Pi_{\mu,i}}{\pi d^3} - \frac{2}{d} [\Pi_{\mu,i} f_{jd} - \delta_{ij} f_{jj} (\Pi_{\mu} - 1)] \\ + 8d\pi (\Pi_{\mu} - 1) f_{id} \varepsilon_j^2 f_{jd} - 2\Pi_{\mu,i} \partial_r f_{jd} \delta_{ij}, \quad (4.6)$$

$$M_i = \frac{\Pi_{\mu,i}}{\pi d^2} + 2\varepsilon_j^2 \Pi_{\mu,k} \phi_{ijk} + \Pi_{\mu,i} f_{jd} + \delta_{ij} f_{jj} (-3\Pi_{\mu} + 1). \quad (4.7)$$

993 **Appendix C: integrals ϕ_{ijk} , Φ_{ijkm} and Υ_{ijkm}**

994 The integrals ϕ_{ijk} , Φ_{ijkm} and Υ_{ijkm} in appendices A and B are defined as follows:

$$\phi_{ijg} = 2\pi \int_0^d f_{ig} f_{jg} r dr, \quad \text{and} \quad \phi_{ijl} = 2\pi \int_d^1 f_{il} f_{jl} r dr, \quad (4.1a)$$

$$\Phi_{ijkg} = 2\pi \int_0^d f_{ig} \partial_r f_{jg} l_{kg} dr, \quad \text{and} \quad \Phi_{ijkl} = 2\pi \int_d^1 f_{il} \partial_r f_{jl} l_{kl} dr, \quad (4.1b)$$

$$\Upsilon_{ijkg} = 2\pi \int_0^d f_{ig} f_{jg} f_{kg} r dr, \quad \text{and} \quad \Upsilon_{ijkl} = 2\pi \int_d^1 f_{il} f_{jl} f_{kl} r dr. \quad (4.1c)$$

995 Inserting the definitions for f_{ij} (2.8), applying once again the convention $f_{kd} = f_{kk}|_{r=d}$,
996 and substituting $\phi \equiv \ln(d)$, these integrals evaluate to:

$$\begin{aligned} \phi_{ijg} &= \frac{\pi}{48} \{d^6 C_{ig} C_{jg} - 6d^4 [C_{ig} f_{jd} + C_{jg} f_{id}] + 48d^2 f_{id} f_{jd}\}, \\ \phi_{ijl} &= \frac{\pi}{96} \left\{ (1-d^2) \left[3(3-d^2) (D_{il} C_{jl} + D_{jl} C_{il}) + 48D_{il} D_{jl} + 2C_{il} C_{jl} (1-d^2)^2 \right. \right. \\ &\quad \left. \left. + 12d^2 \phi \left((2-d^2) (D_{il} C_{jl} + D_{jl} C_{il}) + 8D_{il} D_{jl} [1-\phi] \right) \right] \right\}, \end{aligned} \quad (4.2)$$

$$\begin{aligned} \Phi_{ijkg} &= \frac{\pi}{7680} C_{jg} d^4 \{10 f_{id} [3d^4 C_{kg}^2 - 32d^2 C_{kg} f_{kd} + 96f_{kd}^2] \\ &\quad + C_{ig} [-3d^6 C_{kg}^2 + 30d^4 C_{kg} f_{kd} - 80d^2 f_{kd}^2]\}, \end{aligned} \quad (4.3)$$

$$\begin{aligned} \Phi_{ijkl} &= -\frac{\pi}{276480} \{5D_{il} \{8D_{jl} [1728D_{kl}^2 [d^2(\phi-1)(3+\phi(2\phi-3)) - (\phi^2-3)] \\ &\quad + 27C_{kl} D_{kl} [d^4(3+4\phi(4\phi-3)) - 16d^2(3-6\phi+4\phi^2) + 3(15-8\phi^2)] \\ &\quad + C_{kl}^2 (4d^6(6\phi-1) + 27d^4(1-4\phi) + 108d^2(2\phi-1) + (85-72\phi^2))\} \\ &\quad + C_{jl} [216D_{kl}^2 (d^4(-11+4\phi(11+2\phi(4\phi-7))) + 16d^2(1-2\phi) - 5) \\ &\quad + 16C_{kl} D_{kl} (d^6(7+6\phi(12\phi-7)) - 54d^4(1-2\phi)^2 + 81d^2(1-2\phi) - 34) \\ &\quad + 3C_{kl}^2 (3d^8(8\phi-1) + 16d^6(1-6\phi) + 36d^4(4\phi-1) + 48d^2(1-2\phi) \\ &\quad - 25)\} + C_{il} \{C_{jl} [72C_{kl}^2 (d^2-1)^5 + 40D_{kl}^2 (8d^6(13+6\phi(-4+3\phi)) \\ &\quad - 27d^4(11+4\phi(2\phi-3)) + 216d^2 - 23) + 45C_{kl} D_{kl} (3d^8(8\phi-3) \\ &\quad + 8d^6(7-12\phi) + 12d^4(8\phi-9) + 72d^2 - 11) \\ &\quad + 60D_{jl} (36D_{kl}^2 (d^4(7+4\phi(2\phi-3)) - 16d^2(2+\phi(\phi-2)) + (16\phi+25)) \\ &\quad + 4C_{kl} D_{kl} (d^6(12\phi-5) + 18d^4(2-3\phi) + 9d^2(8\phi-11) + 2(27\phi+34)) \\ &\quad + C_{kl}^2 (3d^8 - 16d^6 + 36d^4 - 48d^2 + (24\phi+25))\}]\}. \end{aligned} \quad (4.4)$$

997 **Appendix D: Additional comparison between model and DNS data**

998 Figure 18 compares time traces of the amplitude and maximal core radius associated
999 with the liquid collar for the case with $\bar{d}=0.87$ in figure 9. Flow conditions in 18 differ
1000 slightly from those in figure 9 in that the wavelength (for both WRIBL simulations and
1001 DNS) is $\Lambda=8R$ instead of $\Lambda=7.73R$. This is because the employed DNS solver Gerris
1002 (Popinet 2009) requires that the length of the computational domain be an integer-valued
1003 multiple of the radius. The DNS was performed with adaptive grid refinement, using a
1004 smallest cell size of $R/2^7$. Because the film trough for this case becomes extremely thin,

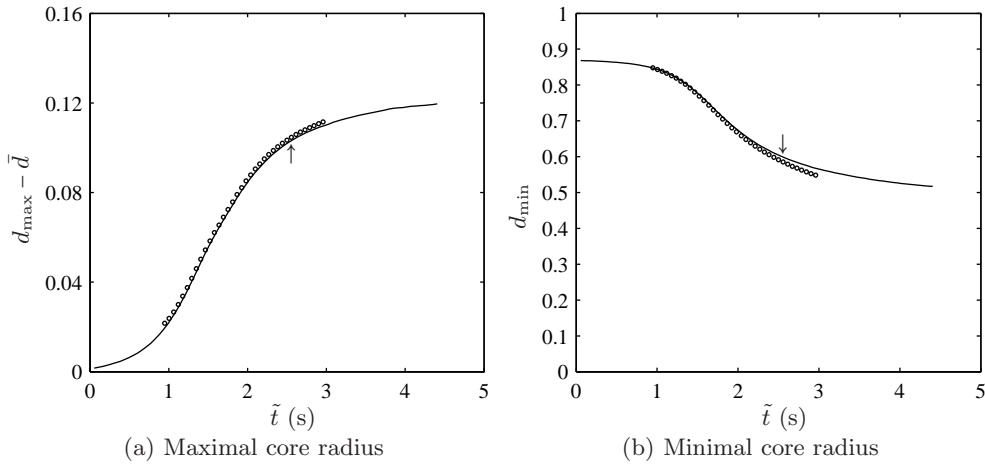


FIGURE 18. Comparison between WRIBL model and DNS: core radius time traces for the case with $\bar{d}=0.87$ in figure 9. In order to accommodate the DNS, both simulations here were performed for a wavelength $\Lambda=8R$, which is an integer-valued multiple of the tube radius and differs slightly from the value in figure 9 ($\Lambda=7.73R$). The arrows mark the time point from which onward the film trough is resolved with less than 3 cells by the DNS (at the last circle-marked data point, the trough contains only two cells).

1005 even this finely-resolved (and very time-consuming) simulation was limited to the time
 1006 range shown by the circles in figure 18. The arrows mark the time from which onwards
 1007 the film trough is radially resolved with less than three cells, while, at the end of the
 1008 range, this resolution becomes inferior to two cells.

REFERENCES

- 1009 ALEKSEENKO, S. V., NAKORYAKOV, V. E. & POKUSAIEV, B. G. 1994 *Wave Flow of Liquid*
 1010 *Films*. Begell House.
- 1011 AUL, R. W. & OLBRICHT, W. L. 1990 Stability of a thin annular film in pressure-driven,
 1012 low-reynolds-number flow through a capillary. *J. Fluid Mech.* **215**, 585–599.
- 1013 BAI, R., KELKAR, K. & JOSEPH, D. D. 1996 Direct simulation of interfacial waves in a high-
 1014 viscosity-ratio and axisymmetric core-annular flow. *J. Fluid Mech.* **327**, 1–34.
- 1015 BIAN, S., TAI, C.-F., HALPERN, D., ZHENG, Y. & GROTBURG, J. B. 2010 Experimental study
 1016 of flow fields in an airway closure model. *J. Fluid Mech.* **647**, 391–402.
- 1017 BROOKE BENJAMIN, T. 1957 Wave formation in laminar flow down an inclined plane. *J. Fluid*
 1018 *Mech.* **2**, 554–574.
- 1019 CAMASSA, R., FOREST, M. G., LEE, L., OGROSKY, H. R. & OLANDER, J. 2012 Ring waves as
 1020 a mass transport mechanism in air-driven core-annular flows. *Phys. Rev. E* **86** (6), 066305.
- 1021 CHEN, K. P. & JOSEPH, D. D. 1991 Long wave and lubrication theories for core-annular flow.
 1022 *Phys. Fluids* **3** (11), 2627–2679.
- 1023 DAO, E. K. & BALAKOTAIAH, V. 2000 Experimental study of wave occlusion on falling films in
 1024 a vertical pipe. *AIChE J.* **46** (7), 1300.
- 1025 DELAUNAY, C. 1841 Sur la surface de révolution dont la courbure moyenne est constante. *Journal*
 1026 *de Mathématiques Pures et Appliquées* **6**, 309–320.
- 1027 DIETZE, G. F. & RUYER-QUIL, C. 2013 Wavy liquid films in interaction with a confined laminar
 1028 gas flow. *J. Fluid Mech.* **722**, 348–393.
- 1029 D’OLCE, M., MARTIN, J., RAKOTOMALALA, N., SALIN, D. & TALON, L. 2008 Pearl and mush-
 1030 room instability patterns in two miscible fluids core annular flows. *Phys. Fluids* **20**, 024104.
- 1031 D’OLCE, M., MARTIN, J., RAKOTOMALALA, N., SALIN, D. & TALON, L. 2009 Convec-

- 1032 tive/absolute instability in miscible core-annular flow. Part 1: Experiments. *J. Fluid Mech.*
1033 **618**, 305–322.
- 1034 DROSOS, E. I. P., PARAS, S. V. & KARABELAS, A. J. 2006 Counter-current gas-liquid flow
1035 in a vertical narrow channel - liquid film characteristics and flooding phenomena. *Int. J.*
1036 *Multiphase Flow* **32**, 51–81.
- 1037 EGGERS, J. & DUPONT, T. F. 1994 Drop formation in a one-dimensional approximation of the
1038 navier-stokes equation. *J. Fluid Mech.* **262**, 205–221.
- 1039 EGGERS, J. & VILLERMAUX, E. 2008 Physics of liquid jets. *Rep. Prog. Phys.* **71**, 036601.
- 1040 EVERETT, D. H. & HAYNES, J. M. 1972 Model studies of capillary condensation. *J. Colloid*
1041 *Interface Sci.* **38** (1), 125–137.
- 1042 FRENKEL, A. L., BABCHIN, A. J., LEVICH, B. G., SHLANG, T. & SIVASHINSKY, G. I. 1987
1043 Annular flows can keep unstable films from breakup: nonlinear saturation of capillary in-
1044 stability. *J. Colloid Interface Sci.* **115** (1), 225–233.
- 1045 GAUGLITZ 1988 An extended evolution equation for liquid film breakup in cylindrical capillaries.
1046 *Chem. Eng. Sci.* **43** (7).
- 1047 GOREN, S. L. 1962 The instability of an annular thread of fluid. *J. Fluid Mech.* **12** (2), 309–319.
- 1048 GOSH, MANDAL, DAS & DAS 2009 Review of oil water core annular flow. *Renewable Sustainable*
1049 *Energy Rev.* **13**, 1957–1965.
- 1050 GOVINDARAJAN, R. & SAHU, K. C. 2014 Instabilities in viscosity-stratified flow. *Annu. Rev.*
1051 *Fluid Mech.* **46**, 331–353.
- 1052 GROTEBERG, J. 1994 Pulmonary flow and transport phenomena. *J. Fluid Mech.* **26**, 529–571.
- 1053 GROTEBERG, J. 2011 Respiratory fluid mechanics. *Phys. Fluids* **23**, 021301.
- 1054 HALPERN, D., FUJIOKA, H. & GROTEBERG, J. B. 2010 The effect of viscoelasticity on the
1055 stability of a pulmonary airway liquid layer. *Phys. Fluids* **22**, 011901.
- 1056 HALPERN, D. & GROTEBERG, J. B. 2003 Nonlinear saturation of the rayleigh-instability due to
1057 oscillatory flow in a liquid-lined tube. *J. Fluid Mech.* **492**, 251–270.
- 1058 HAMACHER, H., FITTON, B. & KINGDON, J. AND 1987 *Fluid Sciences and Materials Science*
1059 *in Space*. Springer, Berlin.
- 1060 HAMMOND, P. S. 1983 Nonlinear adjustment of a thin annular film of viscous fluid surrounding
1061 a thread of another within a circular cylindrical pipe. *J. Fluid Mech.* **137**, 363–384.
- 1062 HEIL, M. & HAZEL, A. L. 2011 Fluid-structure interaction in internal physiological flows. *Annu.*
1063 *Rev. Fluid Mech.* **43**, 141–162.
- 1064 HICKOX, C. E. 1971 Instability due to viscosity and density stratification in axisymmetric pipe
1065 flow. *Phys. Fluids* **14** (2), 251–262.
- 1066 HU, H. H. & JOSEPH, D. D. 1989 Lubricated pipelining: stability of core-annular flow. part 2.
1067 *J. Fluid Mech.* **205**, 359–396.
- 1068 JEBSON, R. S. & CHEN, H. 1997 Performances of falling film evaporators on whole milk and a
1069 comparison with performance on skim milk. *J. Dairy Res.* **64**, 57–67.
- 1070 JENSEN, O. E. 2000 Draining collars and lenses in liquid-lined vertical tubes. *J. Colloid Interface*
1071 *Sci.* **221**, 38–49.
- 1072 JOHNSON, M., KAMM, R. D., HO, L. W., SHAPIRO, A. & PEDLEY, T. J. 1991 The nonlinear
1073 growth of surface-tension-driven instabilities of a thin annular film. *J. Fluid Mech.* **233**,
1074 141–156.
- 1075 JOSEPH, D. D., BAI, R., MATA, C., SURY, K. & GRANT, C. 1999 Self-lubricated transport of
1076 bitumen froth. *J. Fluid Mech.* **386**, 127–148.
- 1077 JOSEPH, D. D., CHEN, K. P. & RENARDY, Y. Y. 1997 Core-annular flows. *Annu. Rev. Fluid*
1078 *Mech.* **29**, 65–90.
- 1079 KALLIADASIS, S., RUYER-QUIL, C., SCHEID, B. & VELARDE, M. G. 2012 *Falling Liquid Films*,
1080 *Applied Mathematical Sciences*, vol. 176. Springer Verlag.
- 1081 KAPITZA, P. L. 1948 Wave flow of thin layer of viscous fluid (in Russian). *Zhurn. Eksper. Teor.*
1082 *Fiz.* **18** (1), 3–28.
- 1083 KERCHMAN, V. 1995 Strongly nonlinear interfacial dynamics in core-annular flows. *J. Fluid*
1084 *Mech.* **290**, 131–166.
- 1085 KOURIS, C. & TSAMOPOULOS, J. 2001 Dynamics of axisymmetric core-annular flow in a straight
1086 tube. I. the more viscous fluid in the core, bamboo waves. *Phys. Fluids* **13** (4), 841–858.
- 1087 KOURIS, C. & TSAMOPOULOS, J. 2002 Dynamics of the axisymmetric core-annular flow. II. the
1088 less viscous fluid in the core, saw tooth waves. *Phys. Fluids* **14** (3), 1011–1029.

- 1089 LISTER, J. R., RALLISON, J. M., KING, A. A., CUMMINGS, L. J. & JENSEN, O. E. 2006
 1090 Capillary drainage of an annular film: the dynamics of collars and lobes. *J. Fluid Mech.*
 1091 **552**, 311–343.
- 1092 MAYO, L. C., MCCUE, S. W. & MORONEY, T. J. 2013 Gravity-driven fingering simulations
 1093 for a thin liquid film flowing down the outside of a vertical cylinder. *Physical Review E* **87**,
 1094 053018.
- 1095 MCKINLEY, G. H. & RENARDY, M. 2011 Wolfgang von ohnesorge. *Phys. Fluids* **23**, 127101.
- 1096 MEHIDI, N. & AMATOUSSE, N. 2009 Modélisation d'un écoulement coaxial en conduite circulaire
 1097 de deux fluides visqueux. *C. R. Mécanique* **337**, 112–118.
- 1098 NEWHOUSE, L. A. & POZRIKIDIS, C. 1992 The capillary instability of annular layers and liquid
 1099 threads. *J. Fluid Mech.* **242**, 193–209.
- 1100 NOVBARI, E. & ORON, A. 2009 Energy integral method for the nonlinear dynamics of an
 1101 axisymmetric thin liquid film falling on a vertical cylinder. *Phys. Fluids* **21**, 062107.
- 1102 NOVBARI, E. & ORON, A. 2011 Analysis of time-dependent nonlinear dynamics of the axisym-
 1103 metric liquid film on a vertical circular cylinder: Energy integral model. *Phys. Fluids* **23**,
 1104 012105.
- 1105 VON OHNESORGE, W. 1936 Die Bildung von Tropfen an Düsen und die Auflösung flüssiger
 1106 Strahlen. *Z. Angew. Math. Mech.* **16**, 355–358.
- 1107 OLBRICHT, W. L. 1996 Pore-scale prototypes of multiphase flow in porous media. *Annu. Rev.*
 1108 *Fluid Mech.* **28**, 187–213.
- 1109 PAPAGEORGIOU, D. T., MALDARELLI, C. & RUMSCHITZKI, D. S. 1990 Nonlinear interfacial
 1110 stability of coreannular film flows. *Phys. Fluids* **2**, 340–352.
- 1111 PIROIRD, K., CLANET, C. & QUÉRÉ, D. 2011 Detergency in a tube. *Soft Matter* **7**, 7498–7503.
- 1112 POPINET, S. 2009 An accurate adaptive solver for surface-tension-driven interfacial flows. *J.*
 1113 *Comput. Phys.* **228**, 5838–5866.
- 1114 POZRIKIDIS, C. 1999 Capillary instability and breakup of a viscous thread. *Journal of Engineer-*
 1115 *ing Mathematics* **36**, 255–275.
- 1116 PREZIOSI, L., CHEN, K. P. & JOSEPH, D. D. 1989 Lubricated pipelining - stability of core
 1117 annular flow. *J. Fluid Mech.* **201**, 323–356.
- 1118 PUMIR, A., MANNEVILLE, P. & POMEAU, Y. 1983 On solitary waves running down an inclined
 1119 plane. *J. Fluid Mech.* **135**, 27–50.
- 1120 QUÉRÉ, D. 1999 Fluid coating on a fibre. *Annu. Rev. Fluid Mech.* **31**, 347–384.
- 1121 RAYLEIGH, LORD 1892 On the instability of cylindrical fluid surfaces. *Philosophical Magazine*
 1122 **34** (207), 177–180.
- 1123 RIBE, N. 2002 A general theory for the dynamics of thin viscous sheets. *J. Fluid Mech.* **457**,
 1124 255–283.
- 1125 RIBE, N. 2012 Liquid rope coiling. *Annu. Rev. Fluid Mech.* **44**, 249–266.
- 1126 RUYER-QUIL, C. & KALLIADASIS, S. 2012 Wavy regimes of film flow down a fibre. *Phys. Rev.*
 1127 *E* **85**, 046302.
- 1128 RUYER-QUIL, C., KOFMAN, N. & CHASSEUR, D. 2014 Dynamics of falling liquid films. *European*
 1129 *Physical Journal E* **37** (30), 1–17.
- 1130 RUYER-QUIL, C. & MANNEVILLE, P. 2000 Improved modeling of flows down inclined planes.
 1131 *Eur. Phys. J. B* **15** (2), 357–369.
- 1132 RUYER-QUIL, C. & MANNEVILLE, P. 2002 Further accuracy and convergence results on the
 1133 modeling of flows down inclined planes by weighted-residual approximations. *Phys. Fluids*
 1134 **14** (1), 170–183.
- 1135 RUYER-QUIL, C., TREVELYAN, P., GIORGIUTTI-DAUPHINE, F., DUPRAT, C. & KALLIADASIS,
 1136 S. 2008 Modelling film flows down a fibre. *J. Fluid Mech.* **603**, 431–462.
- 1137 SELVAM, B., TALON, L., LESSHAFFT, L. & MEIBURG, E. 2009 Convective/absolute instability
 1138 in miscible core-annular flow. Part 2. numerical simulations and nonlinear global modes. *J.*
 1139 *Fluid Mech.* **618**, 328–348.
- 1140 SHKADOV, V. YA. 1967 Wave flow regimes of a thin layer of viscous fluid subject to gravity.
 1141 *Fluid Dyn.* **2** (1), 29–34.
- 1142 SIEROU, A. & LISTER, J. R. 2003 Self-similar solutions for viscous capillary pinch-off. *J. Fluid*
 1143 *Mech.* **497**, 381–403.
- 1144 SLIM, A. C., BALMFORTH, N. J., CRASTER, R. V. & C., MILLER J. 2009 Surface wrinkling of
 1145 a channelized flow. *Proc. R. Soc. London, Ser. A* **465**, 123–142.

- 1146 SLIM, A. C., TEICHMAN, J. & MAHADEVAN, L. 2012 Buckling of a thin-layer Couette flow. *J.*
1147 *Fluid Mech.* **694**, 5–28.
- 1148 SULEIMAN, M. & MUNSON, B. R. 1981 Viscous buckling of thin fluid layers. *Phys. Fluids* **24**,
1149 1–5.
- 1150 TAI, C.-F., BIAN, S., HALPERN, D., ZHENG, Y., FILOCHE, M. & GROTBORG, J. B. 2011
1151 Numerical study of flow fields in an airway closure model. *J. Fluid Mech.* **677**, 483–502.
- 1152 THIELE, U., TODOROVA, D. V. & LOPEZ, H. 2013 Gradient dynamics description for films of
1153 mixtures and suspensions: Dewetting triggered by coupled film height and concentration
1154 fluctuations. *Phys. Rev. Lett.* **111**, 117801.
- 1155 TIMMERMANS, M.-L. E. & LISTER, J. R. 2002 The effect of surfactant on the stability of a
1156 liquid thread. *J. Fluid Mech.* **459**, 289–306.
- 1157 TRIFONOV, Y. Y. 1992 Steady-state traveling waves on the surface of a viscous liquid film falling
1158 down on vertical wires and tubes. *AIChE J.* **38** (6), 821–834.
- 1159 TRIFONOV, Y. Y. 2010a Counter-current gas-liquid wavy film flow between the vertical plates
1160 analyzed using the Navier-Stokes equations. *AIChE J.* **56** (8), 1975–1987.
- 1161 TRIFONOV, Y. Y. 2010b Flooding in two-phase counter-current flows: Numerical investigation
1162 of the gas-liquid wavy interface using the Navier-Stokes equations. *Int. J. Multiphase Flow*
1163 **36**, 549–557.
- 1164 WANG, Q. 2013 Capillary instability of a viscous liquid thread in a cylindrical tube. *Phys. Fluids*
1165 **25**, 014104.
- 1166 WRAY, A. W. 2013 Electrostatically controlled large-amplitude, non-axisymmetric waves in thin
1167 film flows down a cylinder. *J. Fluid Mech.* **736**, R2.
- 1168 YARIN, A. L. & TCHADAROV, B. M. 1996 Onset of folding in plane liquid films. *J. Fluid Mech.*
1169 **307**, 85–99.
- 1170 YIANTSIOS, S. G. & HIGGINS, B. G. 1989 Rayleigh-taylor instability in thin viscous films.
1171 *Physics of Fluids A* **1**, 1484.
- 1172 YIH, C.-S. 1967 Instability due to viscosity stratification. *J. Fluid Mech.* **27** (2), 337–352.